AD

AWARD NUMBER: W81XWH-09-1-0502

TITLE: Breast Cancer-Targeted Nuclear Drug Delivery Overcoming Drug Resistance for Breast Cancer Chemotherapy

PRINCIPAL INVESIGATOR: Maciej Radosz

CONTRACTING ORGANIZATION: University of Wyoming
Laramie, WY 82071

REPORT DATE: September 2013

TYPE OF REPORT: Final

PREPARED FOR: U.S. Army Medical Research and Material Command
Fort Detrick, Maryland 21702-5012

# REPORT DOCUMENTATION PAGE

*Form Approved*
*OMB No. 0704-0188*



| **1. REPORT DATE** *(DD-MM-YYYY)* | **2. REPORT TYPE** | **3. DATES COVERED** *(From - To)* |
|---|---|---|
| September 2013 | Final | 1 Sep 2009 - 31 Aug 2013 |

**4. TITLE AND SUBTITLE**
Breast Cancer-Targeted Nuclear Drug Delivery
Overcoming Drug Resistance for Breast Cancer Chemotherapy

**5a. CONTRACT NUMBER**

**5b. GRANT NUMBER**
W81XWH-09-1-0502

**5c. PROGRAM ELEMENT NUMBER**

**6. AUTHOR(S)**
Maciej Radosz, Youqing Shen

**5d. PROJECT NUMBER**

**5e. TASK NUMBER**

**5f. WORK UNIT NUMBER**

**7. PERFORMING ORGANIZATION NAME(S) AND ADDRESS(ES)**
University of Wyoming
Laramie, WY 82071

**8. PERFORMING ORGANIZATION REPORT NUMBER**

**9. SPONSORING / MONITORING AGENCY NAME(S) AND ADDRESS(ES)**
U.S.Army Medical Research and Material Command
Fort Detrick, Maryland 21702-5012

**10. SPONSOR/MONITOR'S ACRONYM(S)**

**11. SPONSOR/MONITOR'S REPORT NUMBER(S)**

**12. DISTRIBUTION / AVAILABILITY STATEMENT**
Approved for public release

**13. SUPPLEMENTARY NOTES**

**14. ABSTRACT**

Breast cancer cells drug resistance mechanisms are the major factors to reduce the cytotoxic effects and even the chemotherapeutic efficacy of anti-cancer drugs. Nanocarriers for drug delivery based on the EPR effect targeted to cell cytosol subject to various intracellular drug-resistance mechanisms which limited their access to the cell nuclei and mitigated the pharmacological actions of DNA-damaged anti-cancer drugs. We developed various kinds of nuclear-*t*argeted *c*harge-*r*eversal *n*anoparticles (TCRNs) which can directly localize and release drug molecules into the nucleus, circumventing both the membrane-associated multidrug resistance and the intracellular drug resistance mechanisms. The cationic primary amines of TCRNs are amidized as acid-labile β-carboxylic amides to shield the positive charges in blood circulation, but hydrolyzed to regenerate once in cancer cells' acidic lysosomes, leading to the TCRNs escape from the lysosomes and traverse into the nucleus. The *in vitro* and *in vivo* administrations of TCRNs exhibited higher antitumor efficacy and fewer side effects, showing great promises for TCRNs in future applications.

**15. SUBJECT TERMS**
Nuclear Drug Delivery

| **16. SECURITY CLASSIFICATION OF:** U | | | **17. LIMITATION OF ABSTRACT** | **18. NUMBER OF PAGES** | **19a. NAME OF RESPONSIBLE PERSON** USAMRMC |
|---|---|---|---|---|---|
| **a. REPORT** | **b. ABSTRACT** | **c. THIS PAGE** | UU | 50 | **19b. TELEPHONE NUMBER** *(include area code)* |

# Table of Contents

**Introduction**

We worked according to the TASKs in the SOW:

STATEMENT OF WORK

Breast Cancer-Targeted Nuclear Drug Delivery Overcoming Drug Resistance for Breast Cancer Chemotherapy
University of Wyoming, 1000 E Univ Ave, Laramie, Wyoming

Maciej Radosz (PI)
Youqing Shen, Ph.D. (Co-PI)
William J. Murdoch, Ph.D. (Co-PI)

TASK 1. To synthesize and optimize folic-acid– or LHRH-functionalized charge reversal nanoparticles (12 Months):

a. Synthesize linear polyethyleneimine (PEI, Mn ~0.8-10kDa) by ring-opening polymerization.
b. React the PEI with proper 5-membered ring-anhydrides to prepare charge-reversal PEIs (PEI/amides), characterize and optimize their charge-reversal kinetics.
c. Introduce folic acid or LHRH to the PEI/amides using a post-reaction method.
d. Fabricate and characterize TCRNs.
e. Load drugs doxorubicin (DOX), camptothecin (CPT) and other drugs for breast cancer to TCRNs.

Milestone 1: To obtain the FA- and LHRH-functionalized TCRNs with optimal charge-reversal kinetics, targeting group density, size, and drug loading.

TASK 2. To in vitro evaluate the TCRNs for breast cancer chemotherapy (12 Months):

a. In vitro test drug release profile at pH 7.4.
b. Test stability in blood.
c. In vitro test cellular binding (competitive inhibition method).
d. In vitro test cellular uptake of TCRNs (flow cytometry, confocal laser-light scanning fluorescence microscopy).
e. Intracellular trafficking.
f. In vitro cytotoxicity to breast cancer cells.

Milestone 2: To screen out the TCRNs with the highest in vitro anti-breast cancer activity.

TASK 3. To in vivo evaluate TCRNs' anti-breast cancer efficacy (12 months)

a. In vivo test biodistribution and tumor targeting efficiency using nude mice (about 120 mice).
b. In vivo test and compare anticancer activity using nude mice with ip tumors and sc tumors treated by ip and iv injections (about 200 mice).

Milestone 3: To screen out the TCRNs with the highest in vivo anticancer activity

**Body**

## 1. Background

Breast cancer cells drug resistance mechanisms, including the loss of surface receptors or transporters to slow drug influx, cell-membrane-associated multidrug resistance to remove drugs[1-3], specific drug metabolism or detoxification[4] and intracellular drug sequestration[5], are the major factors to reduce the cytotoxic effects and even the chemotherapeutic efficacy of anti-cancer drugs. Particularly, cancer cells often exhibit an altered pH gradient across different cell compartments to increase the drug-sequestering capacity of the compartments, resulting in only a small percentage of drugs can finally reach the nucleus in drug-resistant cells. Therefore, overcoming the drug resistance mechanisms is the key determinant for achieving higher therapeutic benefits.

Nanocarriers for drug delivery based on the enhanced permeability and retention (EPR) effect[6, 7] have been shown to bypass membrane-associated multidrug resistance and thus had significantly improved drug's cytotoxicity to resistant cells. However, nanocarriers targeted to cell cytosol subject to various intracellular drug-resistance mechanisms which limited their access to the cell nuclei and mitigated the pharmacological actions of DNA-damaged anti-cancer drugs.

Therefore, a nuclear-targeted nanocarrier which can directly localize and release drug molecules into the nucleus would circumvent both the membrane-associated multidrug resistance and the intracellular drug resistance mechanisms, and thereby to make the nuclear drug exert its DNA-damaged function to induce the cell apoptosis. Motivated by the polyethyleneimine (PEI)-mediated gene delivery, in which cationic PEI condenses large DNA molecules into nanoparticles and leads them to efficiently enter the nucleus, we developed various kinds of nuclear-*t*argeted *c*harge-*r*eversal *n*anoparticles (TCRNs) to overcome breast cancer drug resistance. The cationic primary amines of TCRNs are amidized as acid-labile β-carboxylic amides to shield the positive charges in blood circulation, but hydrolyzed to regenerate once in cancer cells' acidic lysosomes, leading to the TCRNs escape from the lysosomes and traverse into the nucleus.

We firstly developed linear PEI based TCRN, LPEI/DM-PCL, and demonstrated its breast cancer nuclear-targeted charge-reversal capability. The folic acid (FA) was introduced to the nanoparticle by a comicellization of TCRN and DSPE-PEG-folate to form FLPEI/DM-PCL. But the ability of the PEI to disrupt the

endosome/lysosome membrane was found not very effective. Thus, we employed polyhistidine (PolyHis) to fabricate another TCRN because PolyHis has a strong fusogenic activity in addition to pH-sensitive ability and biodegradability. Its imidazole groups are only partially protonated at physiological pH but fully protonated at lysosomal/endosomal pH[8, 9], leading to the efficient disruption of endosomes/lysosomes[10]. Similarly, the FA group was introduced to the PCL-PolyHis$^{-S}$ nanoparticle by mixing the FA-PEG-PCL at the molar ratio of 10%. Furthermore, we applied the approach to prepare a charge-reversal liposome DOLPEI/amide and a charge-reversal peptide $^{a}$TAT formed $^{a}$TAT-PEG-PCL nanoparticle.

Moreover, we synthesized a series of degradable dendrimers and applied such dendrimers to formulate novel drug delivery systems to improve the limited penetration of anti-cancer drugs within tumor tissues. In addition, a new nanorod-like nanocarrier was prepared and demonstrated be advanced to similar spherical nanocarries. Besides, we reviewed the current achievements as well as proposed new criterions and strategies of translational nanocarriers for cancer chemotherapy.

## 2. Anti-cancer drug delivery by nuclear-targeted charge-reversal nanoparticles (TCRNs)

### 2.1 Polymer design and synthesis

The charge-reversal polymers were designed and synthesized based on a charge-reversal method for the preservation of amines[11]. The polymers with either primary or secondary amines were synthesized by extensively used polymerization approaches. The cationic amines were amidized as acid-labile β-carboxylic amides and hydrolyzed to regenerate once in an acidic pH environment. The substituent on the β-carboxylic amide in different polymers and the molecular weight of polymers determined the hydrolysis kinetics of the amide and the toxicity of materials[12]. The reaction conditions and purification methods were optimized as to make the final products with fewer by-products and less toxic to cells. The polymer structures were determined by NMR and the molecular weights were determined by GPC.

Taken the charge-reversal linear PEI (LPEI) based nanoparticle as a typical example. The TCRN with a negative-to-positive charge-reversal LPEI shell triggered by the lysosomal (pH 4–5) for nuclear drug delivery was synthesized as shown in Figure 1. The secondary amines in the LPEI block were partially amidized to acid-labile amides to inhibit its interactions with cells before reaching tumor tissues, but once at the acidic

lysosomes, the amides quickly hydrolyzed and regenerated LPEI. LPEI is known to be able to rupture lysosomes via the "proton-sponge" effect[13]. Thus, the regenerated LPEI could help the nanoparticles to escape from the lysosomes into the cytosol, and further lead them to localize in the nucleus. Accordingly, the 2,3-dimethylmaleic (DM) anhydride amidized LPEI/DM-PCL copolymer was synthesized. PCL with molecular weight of about 2000 was synthesized by the ring-opening polymerization of ε-CL initiated by octanoic acid and the carboxyl end group was activated by N-hydroxysuccinimide to obtain PCL–NHS. LPEI terminated with $NH_2$ with molecular weight of about 1000, 1500 and 2000 was obtained by the ring-opening polymerization of MeOZ followed by hydrolysis in hydrochloride solution. PCL–NHS easily reacted with as light excess of LPEI-$NH_2$ to form a di-block copolymer LPEI–PCL. The free LPEI was removed by dialysis. The structure of the LPEI–PCL was characterized by MALDI-TOF MS spectra (Figure 2A) and $^1$HNMR (Figure 2B).

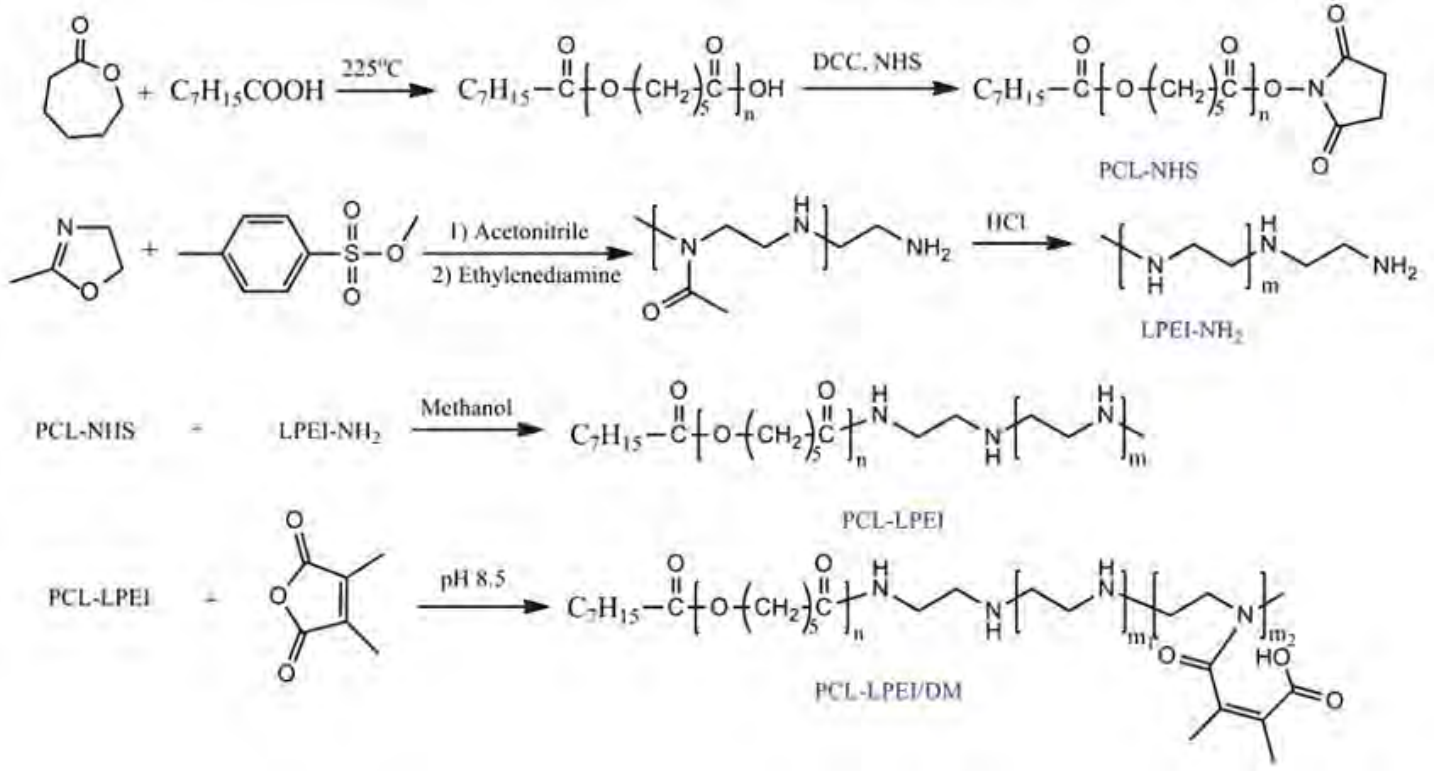


Figure 1. Synthesis of LPEI-PCL block copolymer and the amidization of LPEI by an anhydride DM to form LPEI/DM-PCL copolymer.

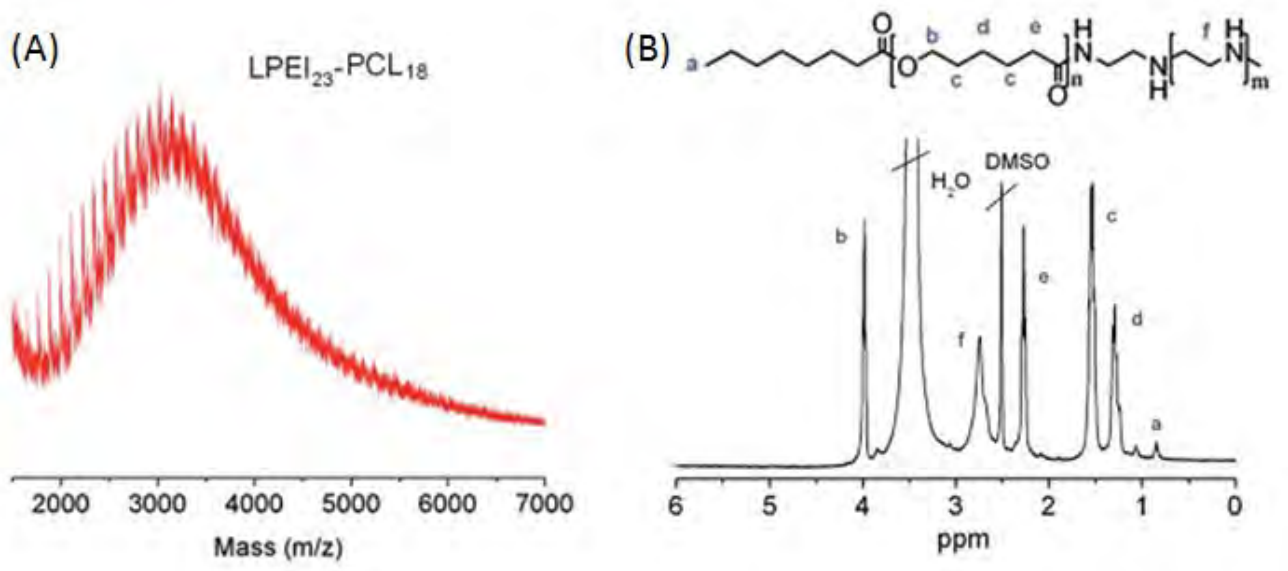


Figure 2. The MALDI-TOF MS spectra of $LPEI_{23}$-$PCL_{18}$ (A) and the $^{1}$HNMR spectra of $LPEI_{23}$-$PCL_{18}$ in DMSO-$d_6$ (B).

As for the synthesis of charge-reversal PolyHis$^{-S}$ based conjugate, using the PolyHis monomer which was first synthesized according to the method reported by Bae et al[14], polycaprolactone (Mn = 2000)-*block*-PolyHis (Mn = 5000) (PCL-PolyHis) copolymer was synthesized (Figure 3). PCL-PolyHis reacted with an excess of succinyl chloride in DMF and amidized the imidazole amine into succinoamide, producing PCL-succino-amidized PolyHis (PCL-PolyHis$^{-S}$).

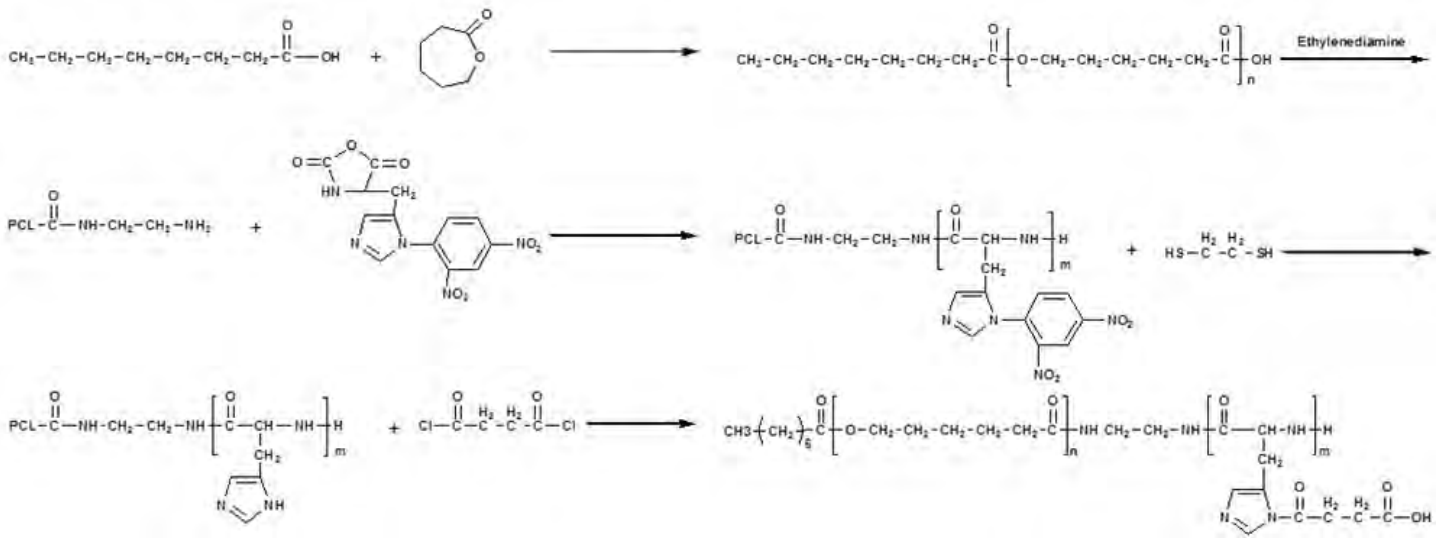


Figure 3. Synthesis of the PCL-block-PolyHis and its amidized product PCL-PolyHis$^{-S}$.

As for the synthesis of charge-reversal liposome, the dioctadecylamino polyMeOz (DOPMeOz) was firstly synthesized via living cationic polymerization of 2-methyl-2-oxazoline (MeOz) terminated with dioctadecylamine[15]. The resulting DOPMeOz was hydrolyzed in 10% hydrochloride solution and produced DOLPEI after adjusting the reaction solution pH higher than 11. The amines in the LPEI were amidized by the DM anhydride in water at pH 8.5 as reported[12]. The resulting DOLPEI/amide was stable in the basic environment (pH > 8.5).

Similarly, the charge-reversal peptide based conjugate $^{a}$TAT-PEG-PCL was obtained by the amidization of TAT lysine residue amines using an excess of succinyl chloride and were carefully characterized by MALDI-TOF mass spectrometry.

**2.2 Property characterization**

The properties of the TCRNs were evaluated in terms of the critical micelle concentration (CMC), particle size and size distribution, and the charge-reversal kinetics[11]. The size of particles was measured using a Nano-ZS Zetasizer and confirmed by TEM image. All the formed nanoparticles had small CMC (<100 mg/L). The optimized sizes of LPEI/DM-PCL (Figure 4), PCL-PolyHis$^{-S}$, DOLPEI/amide, $^{a}$TAT-PEG-PCL nanoparticles are 90, 133, 145 and 70 nm, respectively.

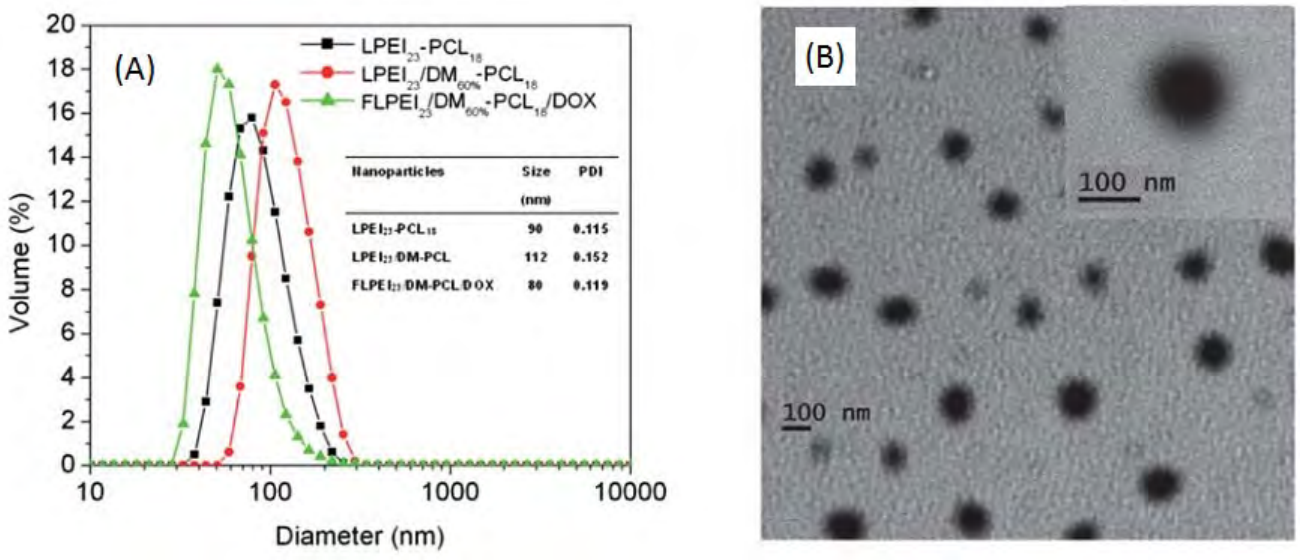


Figure 4. The size distribution of $LPEI_{23}$-$PCL_{18}$, $LPEI_{23}/DM_{60\%}$-$PCL_{18}$ and its DOX-loaded nanoparticles (A). The TEM of $FLPEI_{23}/DM_{60\%}$–$PCL_{18}$/DOX (B).

The TCRNs is expected to be negatively charged at physiological pH (pH 7.4) which inhibits its interaction with cells but should quickly hydrolyze to regenerate the cationic surface at the tumor extracellular pH (pH < 7) or the endosomal/lysosomal pH (pH 4-5) for cellular uptake, endosomal/lysosomal escape, and even nuclear localization. Therefore, the crucial rate of charge-reversal triggered by acid hydrolysis was carefully compared and determined by amidized via different anhydrides. The ζ-potential was measured using phase-analysis light-scattering technology.

For example, the β-carboxylic acid amides of the secondary amine in LPEI from DM was found the best for LPEI, as shown by the time-dependent hydrolysis of LPEI/DM-PCL at pH 11.0, 7.4, 6.0 and 5.0 in Figure 5A. The amide was very stable at the basic condition, for instance at pH 11.0. At pH 7.4, LPEI/DM only hydrolyzed very slowly, about 30% after 40 h. The amide hydrolyzed very fast at acidic pH. The time needed for 50% of LPEI/DM to hydrolyze was 3 h at pH 5.0 and 7.7 h at pH 6.0. LPEI/DM has pendant β-carboxylic acid groups and thus the formed LPEI/DM–PCL nanoparticles were negatively charged at pH 7.4. As the amides hydrolyzed and regenerated the secondary amines, the nanoparticle gradually became positively charged. This charge-reversal was monitored by the nanoparticles' ζ-potentials, as shown in Figure 5B. LPEI/DM–PCL had a ζ-potential of about -25, -12 and -5 at pH 7.4, 6.0 and 5.0, respectively. At pH 7.4, the ζ-potential increased gradually but remained negative even after 40 h. The nanoparticles quickly became positively charged at acidic pH. The time needed to become positively charged was 6.5 h at pH 6.0 and 0.4 h at pH 5.0. These trends are consistent with the hydrolysis results. These data also indicated that LPEI/DM–PCL is capable of negative-to-positive charge reversal once exposed in an acidic condition.

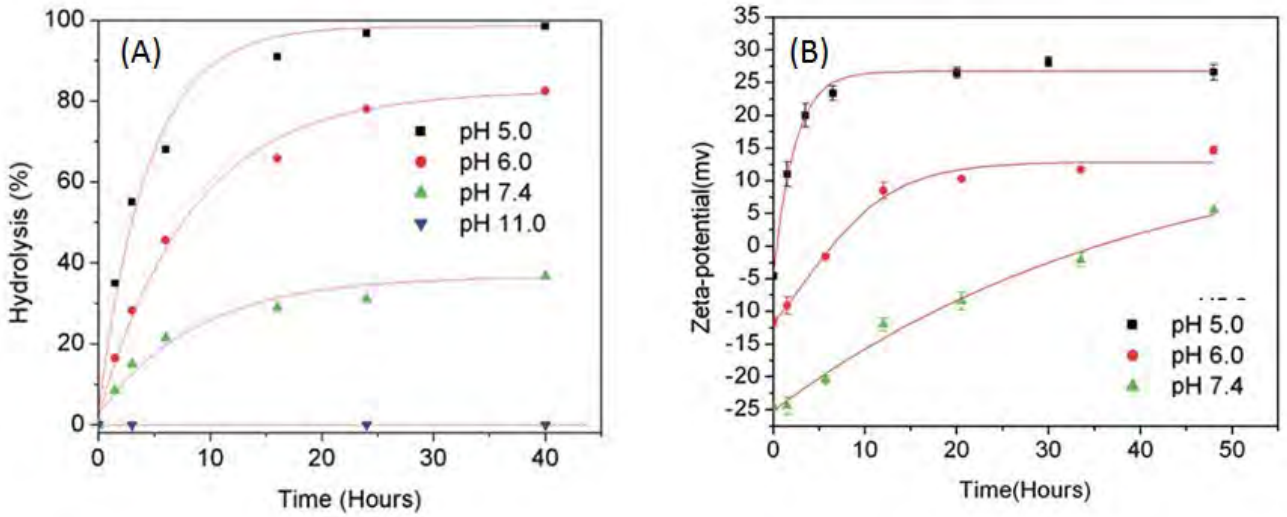


Figure 5. The hydrolysis kinetics of the β-carboxylic amides in $LPEI_{23}/DM_{60\%}$-$PCL_{18}$ at pH 11.0, 7.4, 6.0 and 5.0 in 0.1 M PBS at 37 ºC detected by $^1$HNMR spectra (A). The ζ-potential of $LPEI_{23}/DM_{60\%}$-$PCL_{18}$ micelles as a function of time at pH 7.4, 6.0 and 5.0 (B).

The hydrolysis of the β-carboxylic acid amide of imidazole in PCL-PolyHis$^{-S}$ was also estimated at pH 7.4, 6.0 and 5.0 using NMR (Figure 6A). The amide very slowly hydrolyzed at pH 7.4, less than 5% in 24 h and only 7% in 48 h, while at weakly acidic pH 6.0 or 5.0, the amide hydrolyzed quickly, 50% at pH 6 and 82% at pH 5 in 12 h. As a consequence, the ζ-potential of the nanoparticles gradually became positive (Figure 6B). These results indicated that the PCL-PolyHis$^{-S}$ nanoparticles were negatively charged at the physiological pH and thus suitable for *in vivo* applications but could regenerate the PolyHis block at the acidic pH conditions. Similarly, the DOLPEI/amide liposome and the $^{a}$TAT-PEG-PCL peptide based conjugate also exhibited the charge reversal from negative to positive with the decrease of pH.

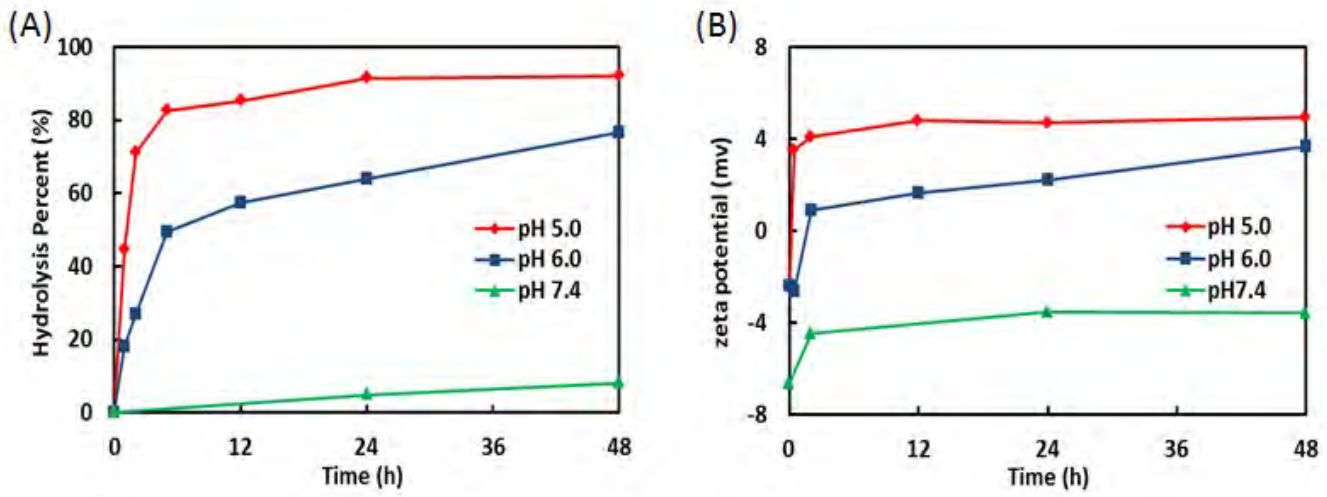


Figure 6. The hydrolytic kinetics curves of the PCL-PolyHis$^{-S}$ at different pH as a function of time detected by NMR (A). The ζ-potential of the PCL-PolyHis$^{-S}$ nanoparticles as a function of time at different pH (B).

**2.3 Drug loading capacity and release**

Anti-cancer drug CPT or DOX was encapsulated in charge-reversal carriers. The drug loading efficiency and content of each carrier were determined using HPLC or UV-Vis spectrometer. For both DOX and CPT, the loading efficiency was proved to be as high as ~90% and the loading content was ~15%. As for the hydrophobic drugs loaded in TCRNs based on hydrophobic-hydrophobic interaction, for instance the DOX·HCl loaded in charge-reversal liposome (DOLPEI/amide/DOX·HCl), the pH-dependent drug-release kinetics were tested at pH 7.4 and 6. As shown in Figure 7, at pH 7.4, only 51.9% of the loaded DOX·HCl was released from the liposome within 12 h while at pH 6.0, 83.3% of that was released within 6 h.

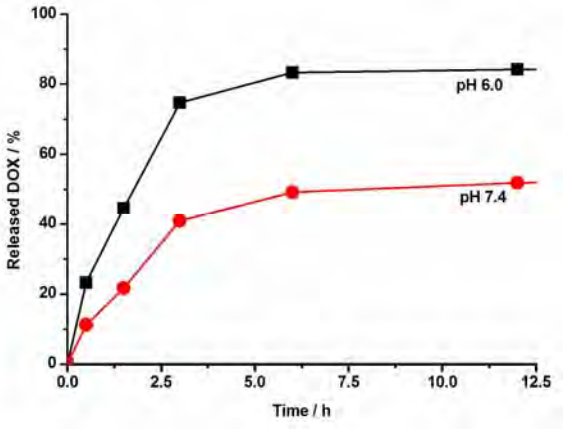


**Figure 7**. The DOX·HCl release kinetics from the DOX·HCl loaded DOLPEI/amide liposomes at pH 7.4 and 6.0 at 37 .

### 2.4 Cellular uptake

At physiological pH, the TCRNs are supposed to have very low interactions with cells. In the acidic solid tumor interstitium, some β-carboxylic acid-amides in the TCRNs are supposed to hydrolyzed and regenerate some amines and thus the TCRNs become partially positively charged, which lead to the conjugate being adsorbed on the negatively charged cell membrane and trigger the cellular uptake. The cellular uptake of the TCRNs by cancer cells was observed using confocal laser light scanning fluorescence microscopy, and further quantitatively measured using flow cytometry[11]. Suitable amount of anti-cancer drugs with its native fluorescence or fluorescent dyes were loaded into nanoparticles. Cells were cultured with nanoparticles and corresponding controls at different timed-intervals. The cells with the fluorescence and the average fluorescence intensity per cell were measured by flow cytometry.

As shown in the flow cytometry result of DOX loaded DOLPEI/amide liposomes (Figure 8), after pretreated at pH 7.4 for 12 h, the DOX fluorescence intensity of DOLPEI/amide/DOX·HCl was comparable to free DOX·HCl, suggesting the DOX·HCl loaded liposome could enter cancer cells as efficiently as free DOX·HCl. After it was pretreated for 12 h at pH 6.0 or 5.0, the DOX fluorescence intensity significantly increased. These results further confirmed that, once in the acidic extracellular fluid of solid tumor tissues, the charge reversal liposome would be able to become positively charged and thus attach to the cell membranes, and then be quickly taken up.

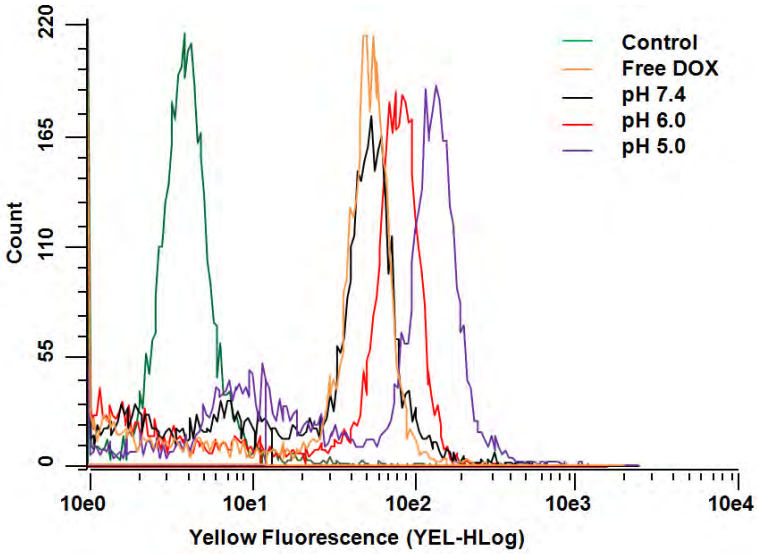


**Figure 8**. The DOX-positive cell population measured by flow cytometry of DOX·HCl and DOX·HCl loaded DOLPEI/amide prehydrolyzed at pH 7.4, 6.0 and 5.0 for 12 h. Referred from the same control cells (green peak, 0.9%). DOX dose was 1 μg/mL$^{-1}$ and the cell counts were 5000.

More convincing proof of the effect of charge reversal on cellular uptake was observed when cancer cells were treated with $^{a}$TAT-PEG-PCL nanoparticle (Figure 9). The PEG-PCL/DOX micelles entered SKOV-3 cells very slowly while the TAT-PEG-PCL/DOX micelles entered cells very quickly. The cellular uptake of $^{a}$TAT-PEG-PCL/DOX micelles was very similar to that of PEG-PCL/DOX and significantly slower than that of TAT-PEG-PCL/DOX, indicating the $^{a}$TAT could not interact with the cells as pristine TAT did. However, once $^{a}$TAT-PEG-PCL micelles were first incubated at pH 5.0 for 8 h, their cellular uptake became as fast as that of TAT-PEG-PCL/DOX, suggesting the recovery of fully functioning TAT moieties on the nanoparticle surface.

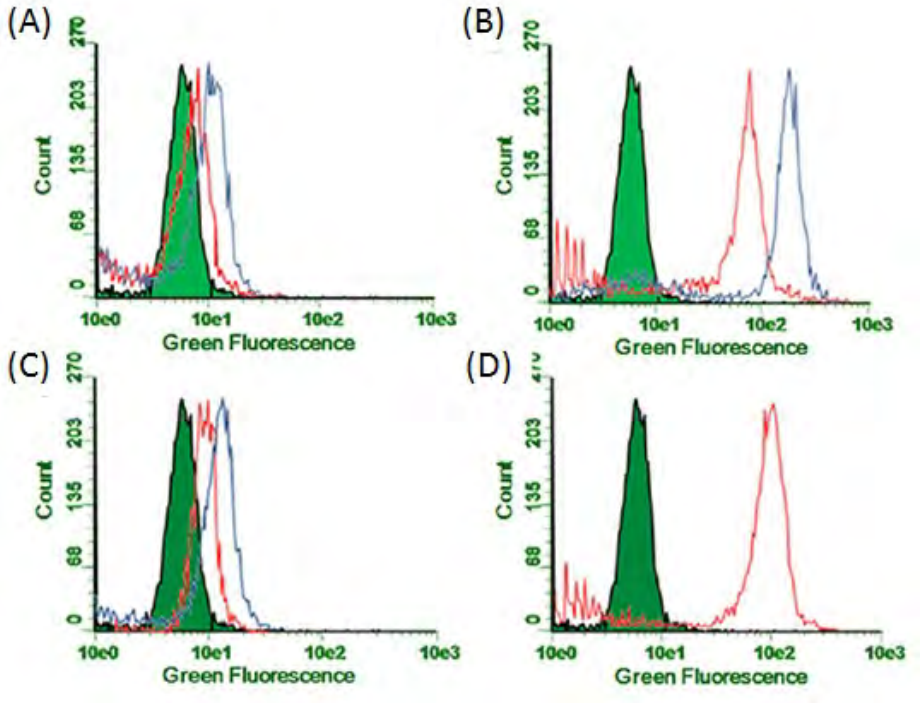


**Figure 9.** DOX-positive cell populations measured by flow cytometry of cancer cells cultured with PEG-PCL/DOX for 1 h (red curve, 3.2%) and 5 h (blue, 15.3%) (A), TAT-PEG-PCL/DOX for 1 h (red curve, 58.6%) and 5 h (blue, 73.7%) (B), [a]TAT-PEG-PCL/DOX for 1 h (red curve,7.8%) and 5 h (blue, 21.2%) (C), and [a]TAT-PEG-PCL/DOX (pre-incubated at pH 5.0 for 8 h) for 5 h (red curve, 64.2%) (D). All of the populations are referenced to the same control cells (green-shaded peaks, 0.8%). The DOX dose was 1 μg/ml.

### 2.5 Intracellular trafficking

To achieve nuclear-targeted drug delivery, the TCRNs should localize in acidic endosome/lysosomes to regenerate the surface positive charges, and subsequently escape from the lysosome and traverse to the nucleus. A subcellular compartment labeling method was used to observe the subcellular distribution of the TCRNs using confocal microscopy. Suitable amount of anti-cancer drugs with its native fluorescence or fluorescent dyes were using as probes to trace the location of nanoparticles. For instance, DOX as a drug and also as a fluorescent dye was loaded into the LPEI based nanoparticles (Figure 10). The nanoparticle images were taken from the DOX fluorescence channel and expressed as red. LysoTracker was used to label late endosomes/lysosomes and displayed as green. The two fluorescence labels overlapped to produce yellow spots, indicating the nanoparticles indeed localized in late endosomes/lysosomes after 6 h cell culturing. Similar endosomal/lysosomal localization of PCL-PolyHis$^{-S}$, DOLPEI/amide and [a]TAT-PEG-PCL were also observed using the method.

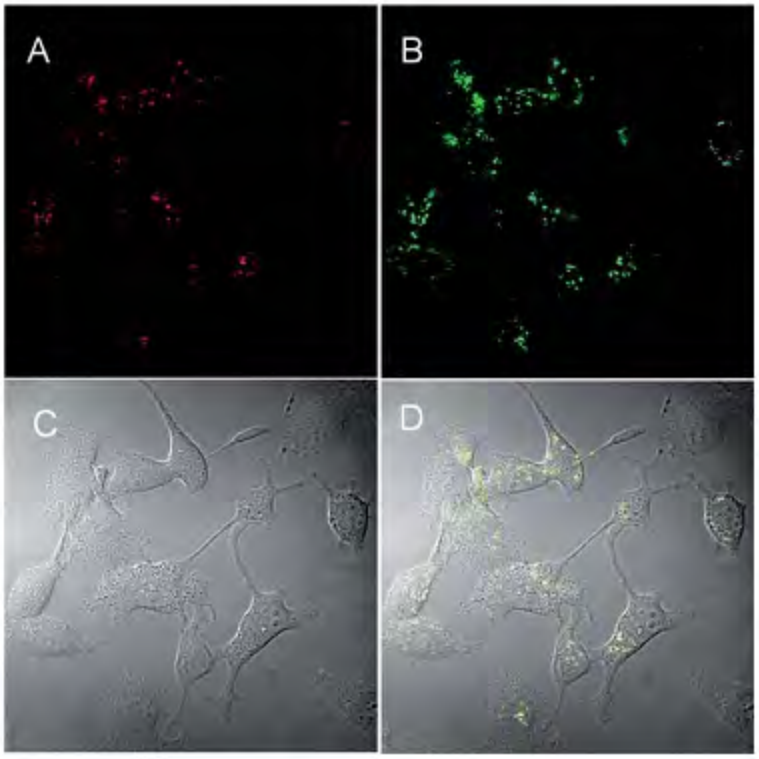


**Figure 10.** Localization of FLPEI/DM-PCL/DOX in endosomes/lysosomes in SKOV-3 cells observed by confocal fluorescence microscopy. FLPEI/DM-PCL/DOX (DOX dose: 2 μg/mL) was cultured with the cells for 6 h. The images were taken from the DOX channel (FLPEI/DM-PCL/DOX) (A), LysoTracker green (B), transmittance channel (C) and their overlay (D).

**2.6 Hemolysis**

The nanoparticles in acidic late endosome/lysosomes (pH 4–5) are expected to regenerate their positive charges and then lyze the lysosomal membrane to escape into the cytosol. The ability of the TCRNs escaping from lysosomes was further tested using a hemolysis assay of sheep red blood cells (RBCs)[16], a measure of a drug carrier's rupture ability to lyze lysosomes. Typically, RBCs were incubated at different polymer concentrations at 37℃ in different PBS buffers for different time intervals. For example, RBCs were incubated with four different LPEI based polymer concentrations in the range of 10-400 mg/mL (Table 1). LPEI-PCL caused 15.1% hemolysis at 100 mg/mL and 41.0% at 400 mg/mL in 2 h. LPEI/DM–PCL without hydrolysis showed no hemolytic ability up to 400 mg/mL. But after being hydrolyzed at pH 6.0 for 24 h LPEI/DM–PCL showed a comparable hemolytic activity to LPEI–PCL at higher concentrations. The results demonstrated that LPEI/DM–PCL would have similar lysosomal lysis ability as LPEI–PCL after regeneration in more acidic lysosomes so that the nanoparticles could escape from the lysosomes.

**Table 1.** Hemolysis activities of the polymers to sheep red blood cells for 120 min incubation at 37 ºC (n=3) (mean ± SD).

| Material | 0.01 mg $mL^{-1}$ | 0.05 mg $mL^{-1}$ | 0.1 mg $mL^{-1}$ | 0.4 mg $mL^{-1}$ |
|---|---|---|---|---|
| LPEI/DM–PCL | 1.49 ± 0.38 | 1.29 ± 0.61 | 1.59 ± 0.86 | 1.63 ± 0.55 |
| LPEI/DM–PCL (hydro 12 h) | 3.37 ± 0.24 | 3.23 ± 0.46 | 2.59 ± 0.23 | 6.25 ± 0.76 |
| LPEI/DM–PCL (hydro 24 h) | 3.01 ± 0.50 | 6.48 ± 0.23 | 10.50 ± 0.77 | 19.54 ± 0.53 |
| LPEI–PCL | 3.64 ± 0.65 | 5.01 ± 1.09 | 15.11 ± 0.67 | 41.00 ± 1.07 |

The hemolysis ability of the PCL-PolyHis$^{-S}$ nanoparticles was also tested. Figure 11 shows that at pH 7.0 PCL-PolyHis$^{-S}$ nanoparticles only lyzed around 5% of the RBCs even at the concentration of 400 μg/mL, but at pH 6.0 could lyzed more than 20% RBCs at the concentration as low as 1 μg/mL. The regenerated PolyHis of the nanoparticles at pH 6.0 ruptured the lysosomes efficiently. At pH 7.0, the nanoparticles could not lyze RBCs even at 100 μg/mL and thus the PCL-PolyHis$^{-S}$ nanoparticles were suitable for the *in vivo* application.

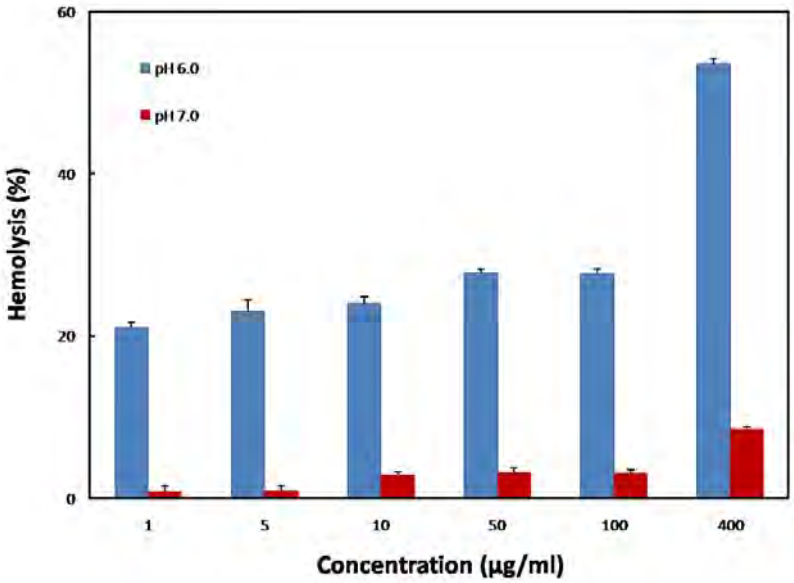


**Figure 11.** The hemolytic activity of PCL-PolyHis$^{-S}$ nanoparticles on RBCs at pH 6.0 and pH 7.4 as a function of concentration (1 h incubation at 37 ℃).

### 2.7 Nuclear localization

After observed the lysosomal localization and proved the lysis ability, the most important nuclear localization of TCRNs was confirmed by observing the colocalization of the nanoparticles and nuclei using confocal microscopy. DOX was loaded in the LPEI based nanoparticles as a fluorescent tracer and expressed as red. DRAQ5 was used to dye nuclei and expressed as blue. As shown in Figure 12, after 6 h cell culturing, some

of the pink spots (generated from the overlapped red and blue signals) in the nuclear region indicated that some DOX were delivered in the nuclei. After further culture for 12 h, more intense DOX-fluorescence was found in the nuclei, indicating more nanoparticles escaped from the acidic lysosome and deliver drugs into the nuclei with longer time. As comparison, free DOX can diffuse into the nuclei of non-drug-resistant cancer cells but the DOX fluorescence intensity in the nuclei was weaker than that treated with the DOX loaded TCRN.

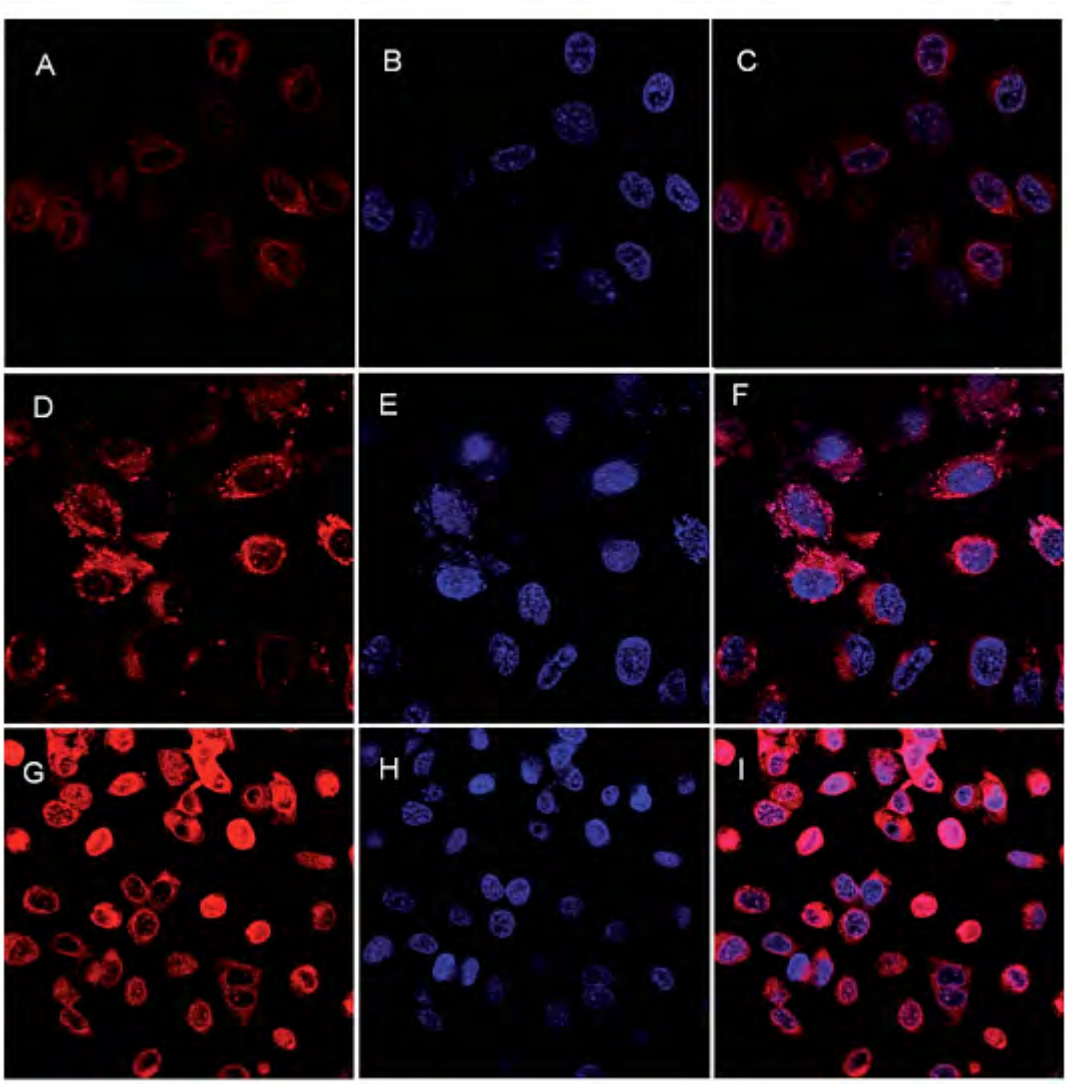


**Figure 12.** Observation of the nuclear localization of free or encapsulated DOX. SKOV-3 cells were cultured with free DOX for 6 h (A-C) and FLPEI/DM-PCL/DOX for 6 h (D-F) or 12 h (G-I) at a DOX dose of 4 μg/mL. Images were taken from the DOX fluorescence channel assigned as red (A, D, and G), DRAQ 5 nuclei dye fluorescence channel assigned as blue (B, E, and H) and the overlay of the images from the two channels (C, F, and I).

In the $^{a}$TAT-PEG-PCL project, nile red, instead of DOX, was used to trace the micelles (Figure 13). The internalized micelles were found initially to be localized in the lysosomes, where $^{a}$TAT could hydrolyze and regenerate TAT. After incubation for 5 h, many micelles were no longer located in the endosomes/lysosomes,

suggesting successful escape from the endosomes/lysosomes. Furthermore, many [a]TAT-PEG-PCL nanoparticles were found punctuated on the nuclear membranes, particularly after 24 h. Thus, such results confirmed that once internalized into a lysosome, the [a]TAT on the nanoparticle was regenerated into TAT, which enabled the nanoparticle escape into the cytosol, traverse to the perinuclear region, and subsequently bind the nuclear pore complexes.

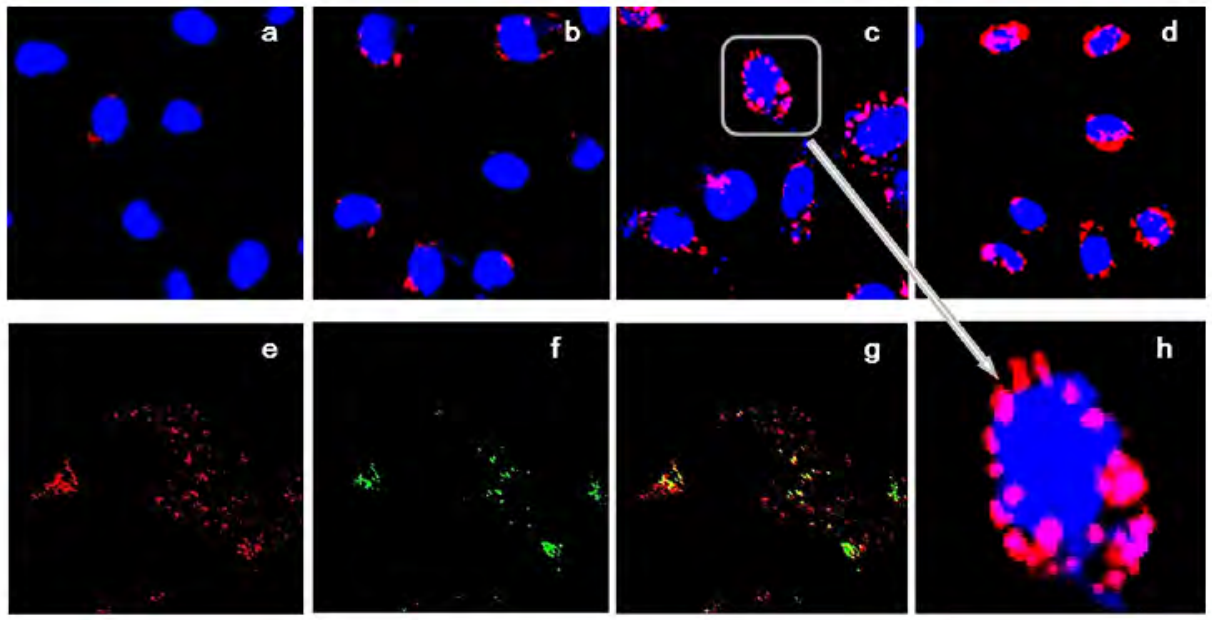


**Figure 13.** Cellular uptake and intracellular localization of [a]TAT-PEG-PCL/nile red nanoparticles observed by confocal microscopy. SKOV-3 cancer cells were cultured with [a]TAT-PEG-PCL/nile red at a nile red dose of 1 μg/ml for 1 (A), 5 (B), 12 (C), and 24 (D) h. An amplification of one cell in (C) is shown in (H). Lysosomal colocalization of [a]TAT-PEG-PCL/nile red in the cells after incubation for 5 h at 37 °C was observed by confocal microscopy through the nile red channel (E) and the LysoTracker green channel (F). The overlap of the images in (E) and (F) is shown in (G). The nuclei were stained with DRAQ5 (blue). Nile red-loaded nanoparticle appear in red and lysosomes stained with LysoTracker in green.

### 2.8 *In vitro* cytotoxicity

The cytotoxicity of drug loaded TCRNs were determined using various cell lines by measuring the cell growth inhibition using a tetrazolium dye (MTT) assay according to our established method[12]. The blank TCRNs are expected to have low cytotoxicity in the body due to the shielding of the positively charged amines. The cells were exposed to the media containing free drug, blank TCRNs, drug loaded TCRNs and drug loaded nanoparticle controls (i.e., nanoparticles similar to TCRNs but without either targeting groups or charge reversibility) at different drug concentrations.

As the MTT results shown in Figure 14, the negatively charged LPEI/DM-PCL had a very low cytotoxicity

while the positively charged LPEI was very toxic as reported. The $IC_{50}$ value of the free DOX to SKOV-3 cells was higher than 10 μg/mL for 24 h treatment and 0.34 μg/mL for 48 h treatment. The $IC_{50}$ of DOX loaded in FLPEI/DM-PCL/DOX to SKOV-3 cells was 0.35 μg/mL for 24 h treatment and 0.12 μg/mL for 48 h treatment. The significantly enhanced cytotoxicity of DOX loaded in the charge-reversal nanoparticles proved the targeted charge-reversal nanoparticles could efficiently cross the cell membrane, escape from the lysosomes, localize and deliver DOX into the nucleus, giving rise to a greater cytotoxicity than free DOX due to bypassing the membrane- and cytosol-associated drug resistance mechanisms.

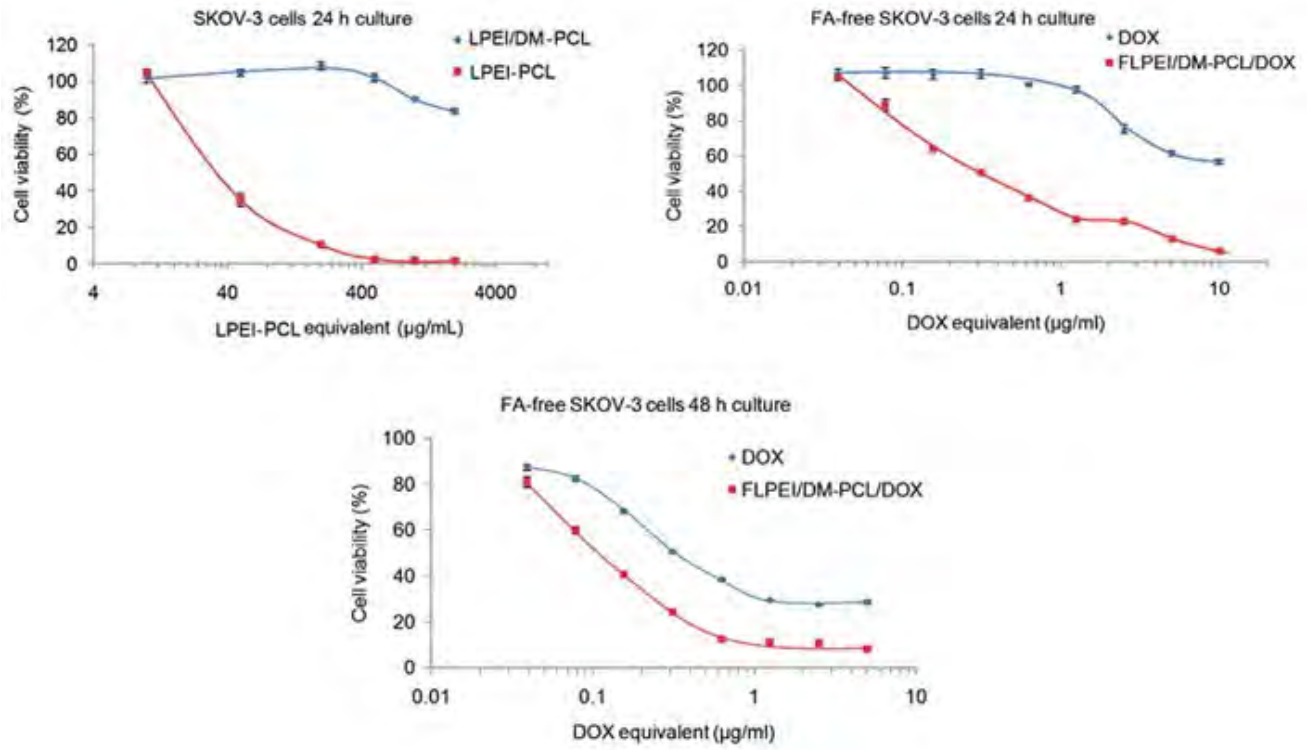


**Figure 14**. The cytotoxicity of LPEI–PCL, LPEI/DM–PCL, DOX and FLPEI/DM–PCL/DOX to SKOV-3 cells estimated by MTT assay. Data represent mean ± SD, n = 5.

The cytotoxicity to SKOV-3 cancer cell line and DOX resistance MCF-7 cancer cell line of CPT or DOX loaded in FA-PCL-PolyHis$^{-S}$ was also evaluated (Figure 15). FA-PCL-PolyHis$^{-S}$/CPT showed a higher cytotoxicity than free CPT at most testing doses. The $IC_{50}$ of the free CPT was about 0.5 μg/mL while it decreased to 0.1 μg/mL once delivered by the FA-PCL-PolyHis$^{-S}$ nanoparticles. As shown in Figure 15B, FA-PCL-PolyHis$^{-S}$/DOX showed higher cytotoxicity than the free DOX in most of the doses to MCF-7 DOX resistant breast cancer cells. Free DOX had almost no dose-dependent cytotoxicity at doses higher than 2 ug/ml and more than 40% cells still survived even at 10 μg/ml dose. In contrast, DOX in the FA-PCL-PolyHis$^{-S}$

nanoparticles quickly reduced cell survival and less than 10% cell survived at 6.8 μg/ml dose. These results further indicated that the nanoparticles could be taken up by the cells efficiently and then delivered the drugs into the nuclei, leading to higher cytotoxicity.

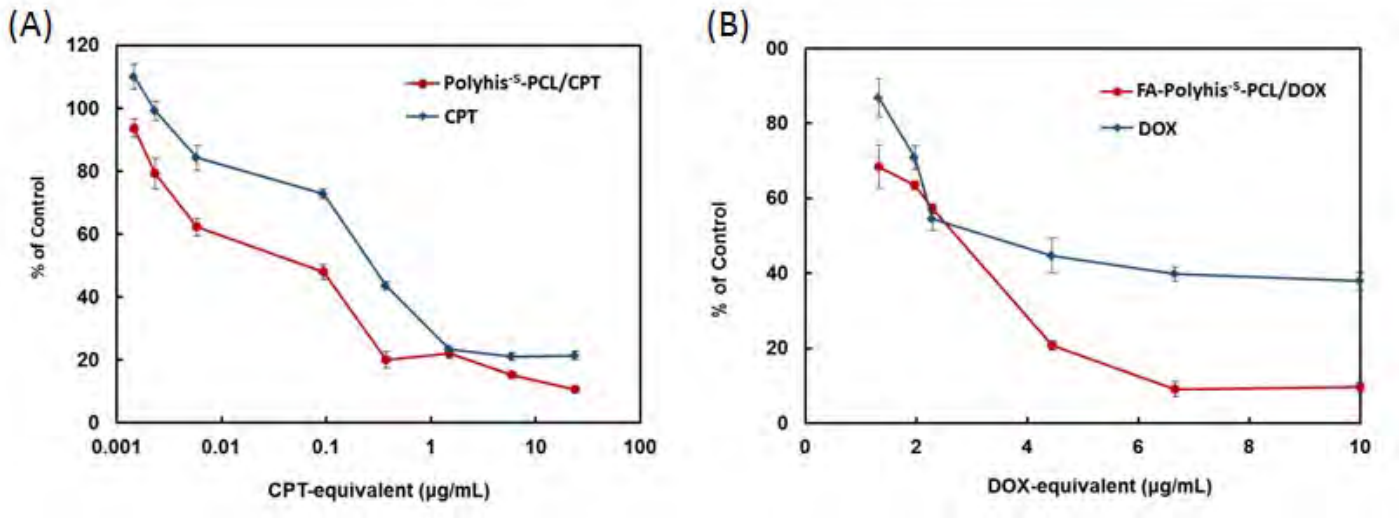


**Figure 15.** The cytotoxicity of CPT and PCL-Polyhis$^{-S}$/CPT to SKOV-3 ovarian cancer cells as a function of CPT dose (A). The cytotoxicity of DOX and FA-PCL-Polyhis$^{-S}$/DOX to MCF-7 DOX resistant breast cancer cells with 24 h treatments and 24 h post treatments (B).

As for the charge-reversal DOLPEI/amide liposome, the blank liposome showed no detectable cytotoxicity to the three types of cancer cells even at high doses (Figure 16). The $IC_{50}$ values of the free DOX·HCl were 0.455, 0.161 and 0.464 μg/mL to SKOV-3, MCF-7 and MCF-7 DOX resistant cells, respectively. However, the DOX·HCl in DOLPEI/amide with the smaller $IC_{50}$ values (0.216 μg/mL for SKOV-3 cells, 0.035 μg/mL for MCF-7 cells and 0.221 μg/mL for MCF-7 DOX resistant cells) exhibited a higher cytotoxicity than free DOX·HCl. This is much advanced to the majority of DOX loaded liposomes previously reported[17, 18]. Similar results were also obtained from the MTT assay of charge reversal [a]TAT-PEG-PCL/DOX nanoparticle.

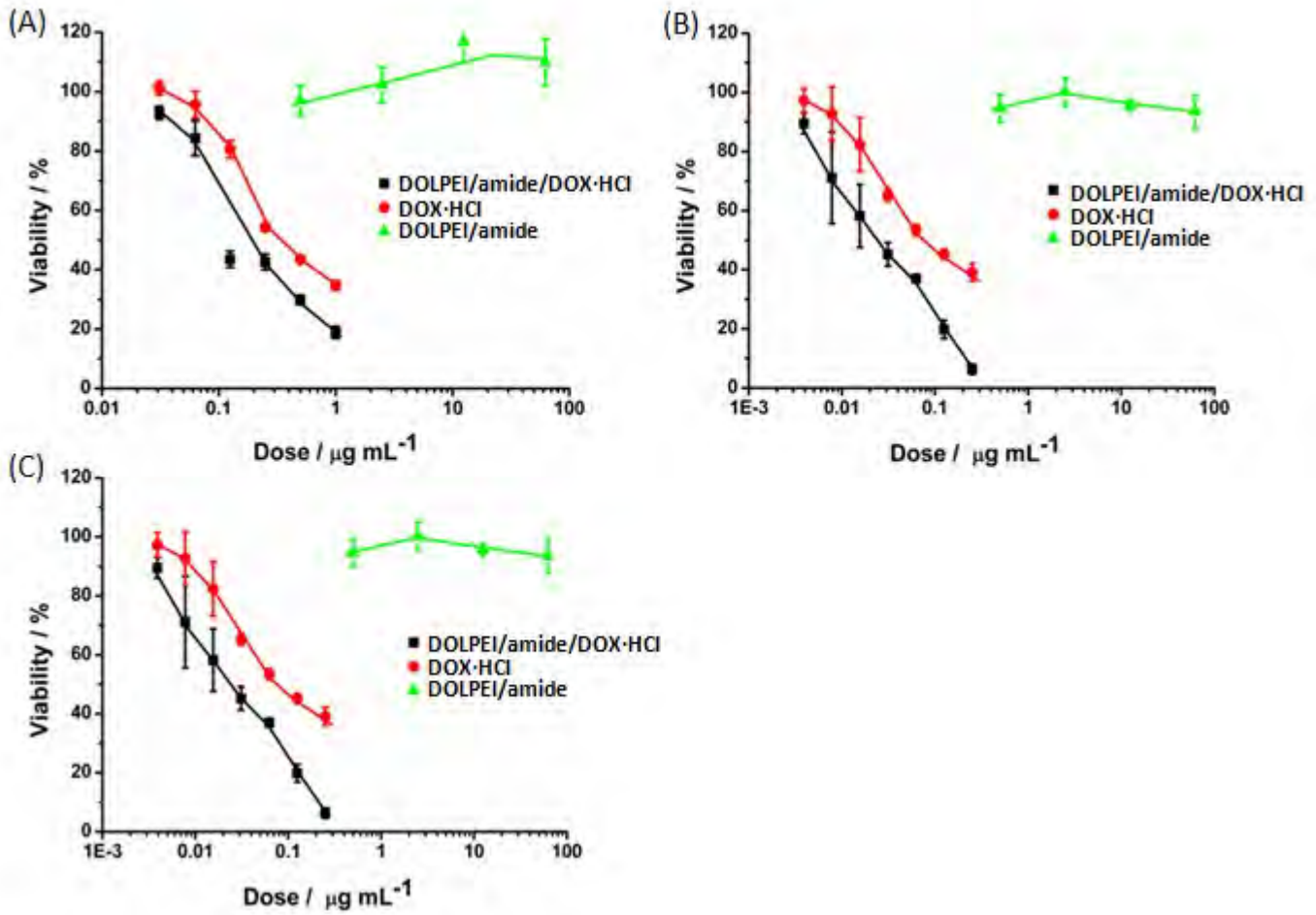


**Figure 16.** The cytotoxicity of DOX·HCl, DOLPEI/amide and DOLPEI/amide/DOX·HCl to SKOV-3 cancer cells (A), MCF-7 (B) and MCF-7 DOX resistant (C) breast cancer cells as a function of the DOX·HCl or DOLPEI/amide dose. Cells were exposed to the indicated drug or liposome for 72 h. Data represent mean ± s.d., n = 5.

### 2.9 *In vivo* administrations

The *in vivo* stability of $^{a}$TAT-PEG-PCL TCRN was evaluated by monitoring its blood clearance (Figure 17A). A near-IR fluorescence dye, DiR, was loaded in the nanoparticles as a tracer since the excitation and emission wavelengths of DiR do not overlap with the auto-fluorescence of blood. As it is shown the i.v.-injected TAT-PEG-PCL nanoparticle was rapidly cleared from the blood stream. In contrast, $^{a}$TAT-PEG-PCL/DiR had a very slow clearance profile similar to that of PEG-PCL/DiR. These results indicated that $^{a}$TAT-PEG-PCL indeed caused no non-specific interactions with the blood component and that the succinyl amides in $^{a}$TAT-PEG-PCL were very stable in blood.

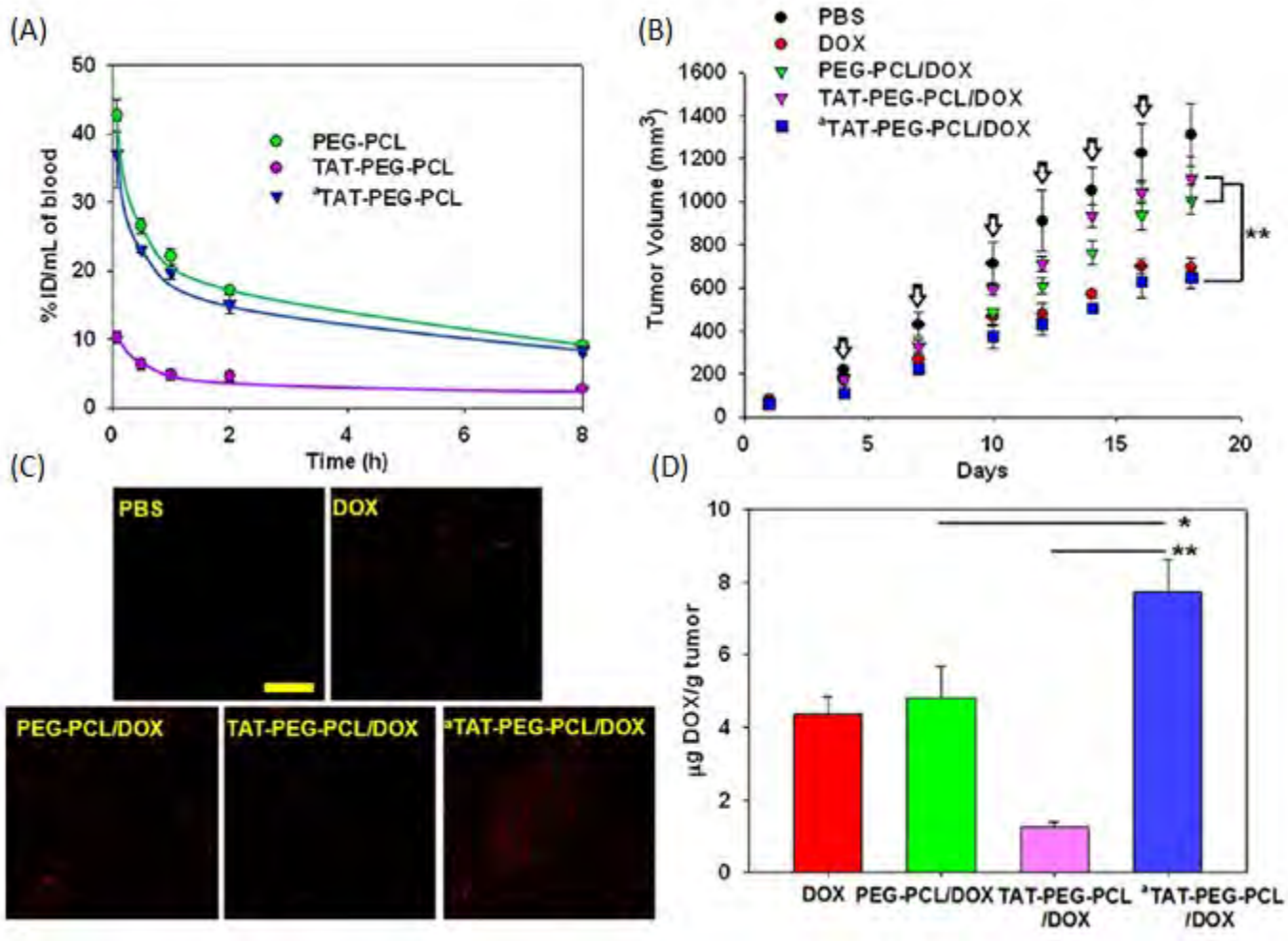


**Figure 17.** Blood clearance of the micelles (A), *in vivo* tumor inhibition of DOX and DOX-loaded micelles (B), and their DOX accumulations in tumors (C & D) as observed by confocal microscopy (C) or as quantitated in terms of micrograms of DOX per gram of tumor tissue (D).

The accumulation in tumor tissues and therapeutic efficacy of DOX delivered by the nanoparticles were subsequently tested using a xenograft tumor model (Figure 17B). The tumor growth of mice administrated with [a]TAT-PEG-PCL/DOX was much slower than that of mice treated with TAT-PEG-PCL/DOX or PEG-PCL/DOX, and this difference became more significant ($p < 0.01$) after day 15. After the mice were sacrificed, the tumors were dissected and weighed. Thus, compared with TAT-PEG-PCL/DOX and PEG/PCL/DOX, [a]TAT-PEG-PCL/DOX showed a significantly ($p < 0.05$) enhanced therapeutic efficacy. Further observation of the tumor sections by confocal microscopy (Figure 17C) showed that there was more DOX in the tumors treated with [a]TAT-PEG-PCL/DOX than in the other tumors. Quantitation of DOX in the homogenized dissected tumors showed that [a]TAT-PEG-PCL/DOX-treated tumors had twice the DOX concentration of tumors treated with PEG-PCL/DOX or DOX and about 8-fold that of tumors treated with TAT-PEG-PCL/DOX (Figure 17D).

## 2.10 Conclusion

In summary, we fabricated, characterized, and *in vitro* and *in vivo* evaluated TCRNs for breast cancer nuclear drug delivery, to overcome breast cancer drug resistance. The LPEI and PolyHis based TCRNs were firstly developed and step-by-step demonstrated their nuclear-targeted charge-reversal capability. We even applied the approach to prepare a charge-reversal DOLPEI/amide liposome and a charge-reversal peptide $^{a}$TAT formed $^{a}$TAT-PEG-PCL nanoparticle. All the chemical structures of charge-reversal carriers were well designed and confirmed as proposed. The physicochemical properties including the size, ζ-potential and pH-triggered hydrolysis of each nanoparticle were carefully measured. Based on the charge reversal process, the detailed intracellular trafficking of the TCRNs were fully traced to elucidate how the nanoparticles across the cell membrane, localize and escape from the lysosome and travel towards the nucleus. The *in vitro* cytotoxicity tests confirmed the blank amidized nanoparticles with negative charges had a very low cytotoxicity, while the drug loaded nanoparticles exhibited higher cytotoxicity than free drug. Further *in vivo* administrations of $^{a}$TAT-PEG-PCL exhibited higher antitumor efficacy and fewer side effects, showing great promises for TCRNs in future *in vivo* applications.

## 3. Synthesis of degradable dendrimers and its applications for drug delivery

Dendrimers are highly branched macromolecules characterized by monodispersity, uniform and controlled sizes and copious surface functionalities[19, 20], which make them ideal nanocarriers for biomedical applications[21]. However, conventional used dendrimers (e.g., PAMAM) are not degradable and carry positive charges on their surface, thus inducing systematic cytotoxicity[22, 23] and rapid blood clearance[24] and hindering their translation to clinical applications. Aliphatic polyester dendrimers, for example, the dendrimers from an $AB_2$-type monomer 2,2-bis(hydroxymethyl)propionic acid (bis-MPA), are biodegradable and biocompatible with very low toxicity and low immunogenicity[25, 26], and thus have been proposed as carriers for biodelivery or *in vivo* imaging[27-31]. However, the synthesis of traditional polyester dendrimers consist of protection/deprotection[32] is tedious and incomplete and thus introduce defects amplified in the subsequent generations[33-37]. Taking advantage of highly efficient thiol/acrylate Michael addition reactions, we developed a simple but efficient strategy to synthesize bis-MPA-based dendrimers without any protection/deprotection steps[38].

### 3.1 Dendrimer design and synthesis

The hydroxyl groups in bis-MPA must be protected first to avoid self-esterification or convert to other functional groups that cannot cause cross-linking[34, 39]. A monomer pair of thioglycerol ($AB_2$) and ACPA ($CD_2$) simplified the reaction requiring no protection/deprotection steps. The Michael addition reaction of thiol−acrylate is almost quantitative without side reactions and considered to be a click reaction in polymer synthesis[40-42] and functionalization[43, 44]. Different from the radical mechanism of the thiol−ene/yne reactions, the thiol−(meth)acrylate reaction does not involve radicals, avoiding side reactions via radical coupling.

The PTA was first reacted with the thiol group in thioglycerol to produce the first-generation dendrimer with eight hydroxyl groups (Figure 18, step i). Pendant hydroxyl groups were esterified with ACPA with catalysis of DIC/DMAP (Figure 18, step ii). Alternating the two steps easily produced the fifth generation of the dendrimers at high overall yields (68%)[38].

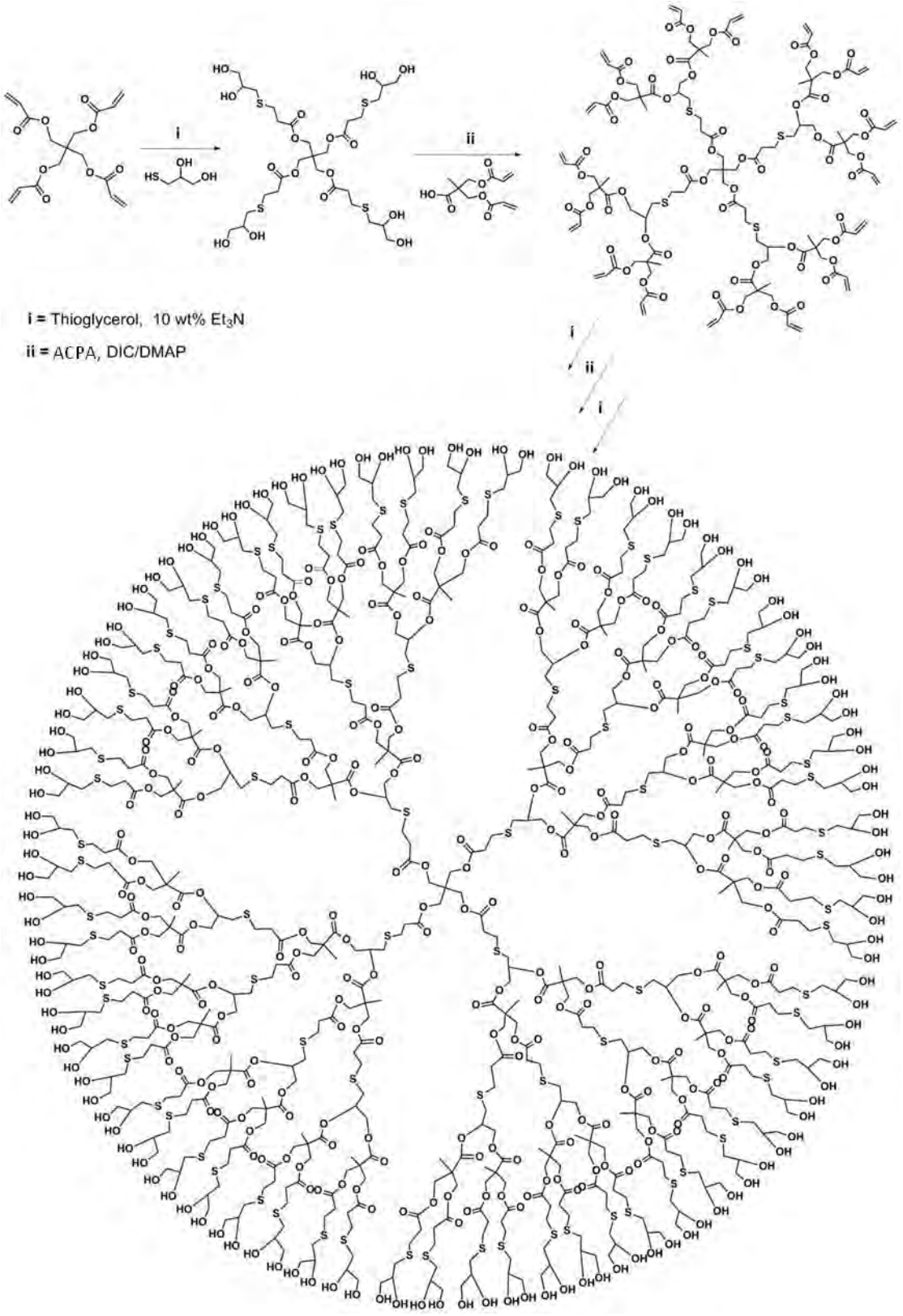


**Figure 18**. Dendrimer synthesis from a $AB_2$ monomer pair 2,2-bis(acryloyloxymethyl)propionic acid (ACPA) and 1-thioglycerol.

Figure 19 shows the MALDI-TOF MS spectra of the reaction solutions. Clearly, the reaction solution in each generation only contained the targeted dendrimer molecules in agreement with the calculated molecular

weight. There were almost no signals of incomplete molecules. The MALDI-TOF spectrum of the fifth generation had a poor resolution due to difficult evaporation as a result of its high molecular weight. However, its GPC trace was as narrow as that of the prior generation, and DLS showed that it had a diameter of 5.2 nm in water with a low PDI, indicating the fifth generation also had similar perfect structure. The typical $^{1}$HNMR spectra of the acrylate- and hydroxyl-terminated dendrimers (G4-$_{64acrylate}$ in $CDCl_3$ and G5-$_{128OH}$ in DMSO-$d_6$) are shown in Figure 20.

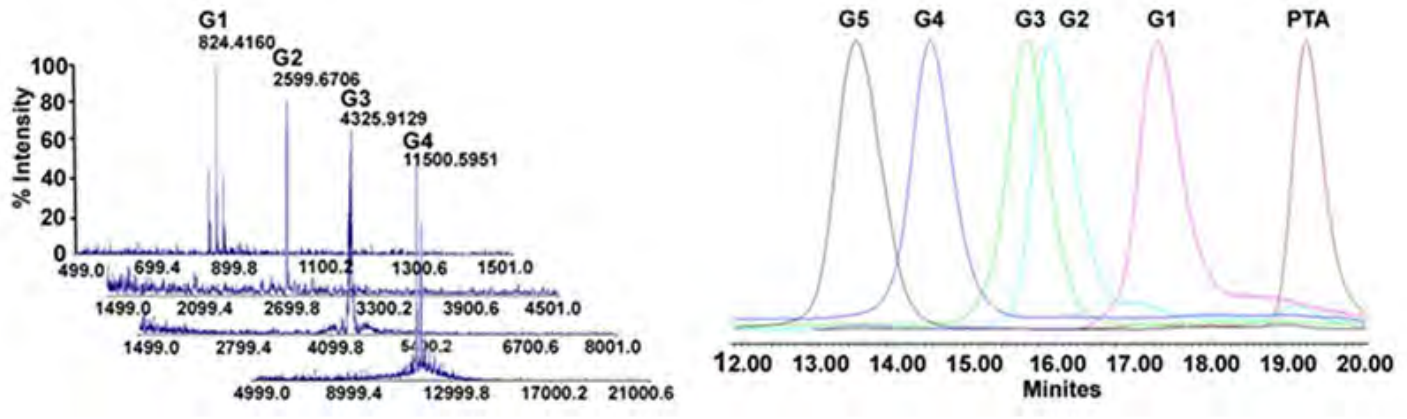


**Figure 19.** Molecular-weight progress of the dendrimers from the reaction of ACPA and thioglycerol measured by (a) MALDI-TOFMS and (b) GPC. The MALDI-TOFMS spectra were obtained from the reaction solutions without any purification.

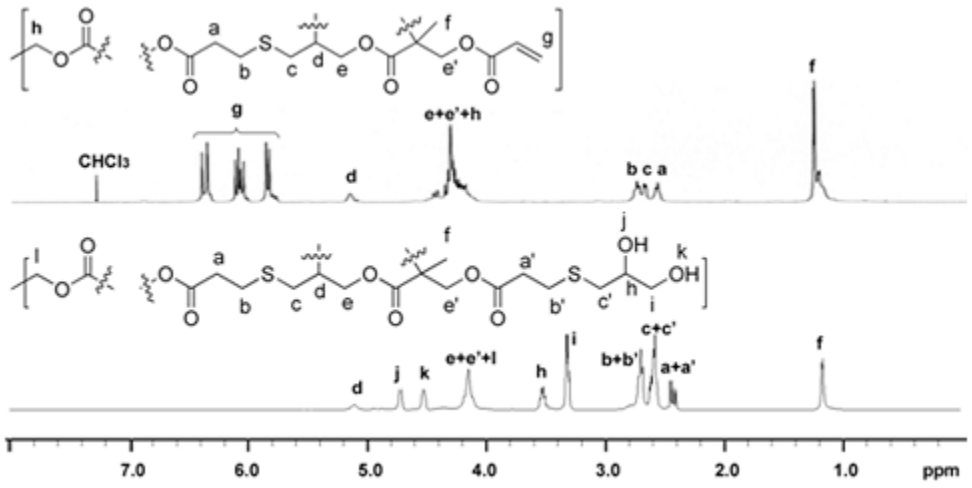


**Figure 20.** $^{1}$HNMR spectra of G4-$_{64acrylate}$ (in $CDCl_3$) and G5-$_{128OH}$ (in DMSO-$d_6$).

### 3.2 Degradable bifunctional dendritic polymers for drug delivery

Generally, all the functional groups in dendrimers are used to construct the dendrimers, and thus there are no reactive groups left in the interior. Therefore, most dendrimers have nonreactive interiors, serving simply as

the skeleton of the nanostructure, and reactive peripheries with functional groups available for functionalization[45, 46]. Thus, drugs, peptides, targeting groups, or polymer chains are generally introduced on the peripheries to obtain dendrimer–drug conjugates[47, 48]. In these dendrimer conjugates, drug moieties tethered to the periphery can contact and thus interact with blood components such as the lipophilic domains of proteins in the blood, causing opsonization. The drug-loading contents of the tethered hydrophobic drugs also cannot be high, generally several percent, to keep the dendrimer conjugates water soluble[49]. When the dendrimer interiors are used to encapsulate drugs, the low drug-loading content and burst release are the two major problems[50].

Therefore, we proposed interior and peripheral bifunctional polyester dendrimers as versatile and biodegradable drug carriers whose interior functional groups might be used for drug conjugation while the periphery might be PEGylated for stealth properties. The fourth-generation dendritic polymer was PEGylated with PEG2k on the periphery and an anticancer drug CPT was tethered in its interior (Figure 21). This interior drug conjugation not only avoids burst drug release, but also hides the drug inside the dendritic polymer, preventing its interaction with serum proteins generally found in drug conjugation on the dendrimer periphery.

Thus, the PEGylated dendritic polymer with interior-conjugated CPT (G4-CPT-PEG) was unimolecular micelles with a core–shell structure. The G4-CPT-PEG with 9.61 wt% or 17.4 wt% CPT was very water soluble. Its average size in DI water was 22.5 or 24.2 nm, respectively. Compared to conventional micelles made from amphiphilic block copolymers, such drug-conjugated dendritic unimolecular micelles also have advantages of fixed drug loading without burst release, small micelle size, well-fined structure, and infinite stability. We compared the cytotoxicity of free CPT, G4-PEG2k, and G4-CPT-PEG (9.61 wt% CPT) to SKOV-3 cancer cells using the MTT assay. G4-PEG2k was not toxic even at high doses. The $IC_{50}$ of the CPT in the G4-CPT-PEG to SKOV-3 cells was 0.499 μg/ml, slightly higher than that of free CPT (0.293 μg/ml), indicating that the CPT conjugated in the dendritic interior could be released inside cell.

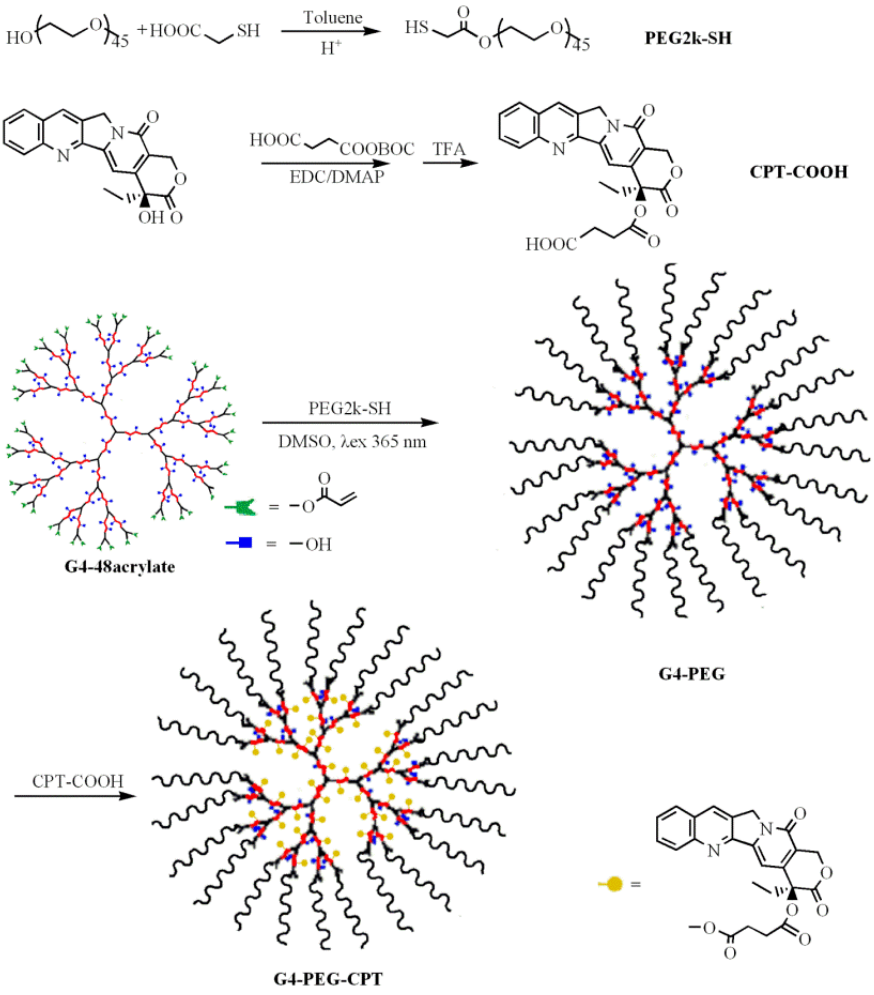


**Figure 21.** Surface PEGylation and interior conjugation of CPT of G4 dendrimer.

### 3.3 Dendrimer/lipid nanoassembly as "cluster bomb" for cascade tumor penetration

Given the reduced adverse effects, the nanosystems crafted to deliver anticancer drugs for chemotherapy do not show as high therapeutic efficacy as we expect[51, 52]. While many factors account for this frustration, the nanosystems' limited penetration into the tumor and thus inaccessibility to the remote tumor cells may be an important determinant[53-55]. Tumors are characterized by unevenly distributed blood vessels—abundant at the invasive edge but few inside the tumor—and tightly packed cells in a dense extracellular matrix[56] with elevated interstitial fluid pressure[57, 58]. Thus, many regions in a tumor are far removed from blood vessels with limited diffusion of nano-sized carriers. Indeed, 100 nm-carriers were found to be restricted at the extravasation sites with little permeation into the tumor[59-61].

Smaller sized nanocarriers, e.g., about 30 nm or less in diameter, could better penetrate tumors[62], yet larger particles have proved to have slower blood clearance and thus longer blood circulation[63] and better tumor

accumulation[62, 64, 65]. Furthermore, stealth nanocarriers are often equipped with targeting ligands that bind receptors on tumor cells or cationic charges to promote their cellular uptake[66]. However, such avid bindings strongly impede nanocarriers' tumor penetration[67]. Therefore, the design of tumor-penetrating nanocarriers must also simultaneously consider other properties including long blood circulation, deep tissue penetration and fast cellular uptake to maximize therapeutic efficacy.

We proposed a long-circulating liposome that could release small nanocarriers capable of deep tumor penetration and fast tumor cell internalization uniting the essential elements of an ideal nanocarrier for cancer-drug delivery. Herein, we present such an example, a liposomal dendrimer nanoassembly (Figure 22). The nanoassembly behaves like a cluster bomb capable of releasing smaller dendrimer nanocarriers (bomblets), uniting the large size needed for long blood circulation and the small size for tumor penetration and fast cellular uptake in the needed region.

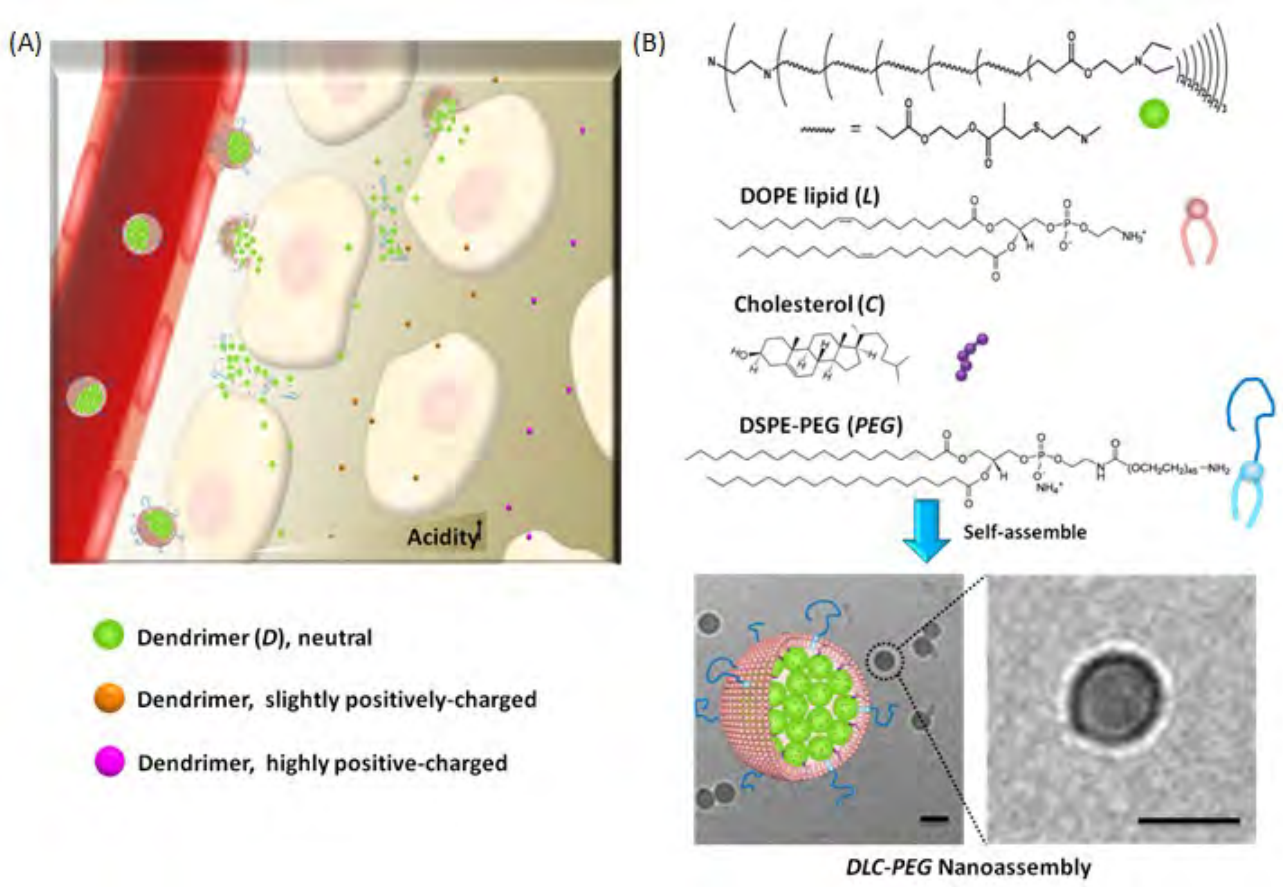


**Figure 22.** Liposomal dendrimer nanoassembly (cluster bomb) concept uniting long blood circulation, deep tumor penetration, and fast cellular uptake (A) and the nanoassembly composition (B). A, The nanoassembly is a PEGylated liposome encapsulated with the dendrimer of several nanometers. It is stealthy and circulates in the blood compartment for tumor targeting via the EPR effect. After extravasating from the tumoral hyperpermeable blood vessels, the nanoassembly sheds its lipid layer and releases the dendrimer, which is small enough to penetrate deep into the tumor regions away from the blood vessels, where the pH is acidic and the

dendrimer becomes positively charged for fast cellular uptake. B**,** The dendrimer was self-assembled with lipids and cholesterol to form the nanoassembly, which was confirmed by cryo-TEM image. The scale bar represents the length of 50 nm.

### 3.3.1 Preparation and characterization of the nanoassembly

The 6$^{th}$-generation nontoxic, degradable polyaminoester dendrimer was synthesized as we previously synthesized[68]. Its diameter was about 5 nm. Its internal cavities were hydrophobic and hence could efficiently encapsulate hydrophobic anticancer drugs[69]. Furthermore, its periphery was functionalized with 2-(*N*,*N*-diethylamino)ethyl termini to render it pH dependence. Its zeta-potential was 3.2 mV at pH 7.4, 5.4 mV at pH 7.0 and 7.0 mV at pH 6.5. Hence, the dendrimer could be quickly internalized at acidic pH, thereby shipping drugs by bypassing the cell multidrug resistance. A phospholipid, 1,2-dioleoyl-sn-glycero-3-phosphoethanolamine (DOPE), chosen for its fusogenic characteristics[70], was used for release of dendrimers within tumor. A PEGylated lipid, 1,2-distearoyl-*sn*-glycero-3-phosphoethanolamine-N-[amino(polyethylene glycol)-2000] (DSPE-PEG), and cholesterol were added to give the nanoassembly stealth properties[71] and stability[72, 73] while in the blood compartment.

The self-assembly of the dendrimer (*D*) with DOPE lipid (*L*), cholesterol (*C*) and DSPE-PEG (*PEG*) was fine tuned in terms of the size, zeta-potential, and stability of the formed *DLC-PEG* nanoassembly. An optimal PEGylated *DLC* nanoassembly (*DLC-PEG*) was formed at a *D*/*L*/*C*/*PEG* molar ratio of 1/60/60/1.5 with a size of 30 ± 2 nm (PDI = 0.163) and a zeta-potential of –9.1 ± 0.5 mV. In 10 wt% bovine serum albumin solution at 37 °C, the *DLC-PEG* was stable for a prolonged time while assemblies without the cholesterol and DSPE-PEG components quickly collapsed.

The nanoassembly structure was further probed using a fluorescence quenching approach[74]. A fluorescence dye, FITC, was tethered to the dendrimer ($^{FITC}$dendrimer or $^{FITC}$*D*), and the $^{FITC}$dendrimer was used to fabricate the labeled nanoassembly, $^{FITC}$*DLC-PEG*. The FITC fluorescence peak at 530 nm in free $^{FITC}$dendrimer shifted to 520 nm after it assembled into $^{FITC}$*DLC-PEG* due to the hydrophobic environment. Gold nanoparticles (AuNPs, 4 nm) are known to quench the fluorescence of FITC and are of a size that cannot diffuse though a lipid layer. Thus, in solution the fluorescence of $^{FITC}$dendrimer was gradually quenched upon adding AuNPs. However, adding AuNPs to the $^{FITC}$*DLC-PEG* nanoassembly solution only slightly reduced the fluorescence

intensity. This suggests that some free $^{FITC}$dendrimer molecules were in the solution and quenched by AuNPs, but most of them were inaccessible to the 4 nm AuNPs, confirming that a lipid layer capsulated most $^{FITC}$dendrimer molecules. We calculated the percentage of dendrimer encapsulated in *DLC-PEG* nanoassembly to be 82%.

### 3.3.2 Drug delivery by dendrimer/lipid nanoassembly

DOX employed as a model drug was loaded into the dendrimer in the *DLC-PEG* nanoassembly by first loading DOX into the dendrimer and using the dendrimer/DOX to fabricate the nanoassembly. The resulting DOX-loaded *DLC-PEG* (*DLC-PEG*/DOX) had a slightly larger diameter, 45 ± 5 nm and a DOX loading content of 9 ± 2 wt%. DOX slowly released from *DLC-PEG* indicating that the dendrimer and lipid synergistically suppressed burst release. The cellular uptake of *DLC-PEG* into SKOV-3 ovarian cancer cells was observed using confocal microscopy. The dendrimer was labeled with FITC and its fluorescence was assigned green; some DOPE was labeled with rhodamine (RHoB) and its fluorescence was assigned red. Thus, the dual-labeled nanoassembly, $^{FITC}D^{RHoB}$*LC-PEG*, was seen as yellow spots. As illustrated in Figure 23A, after $^{FITC}D^{RHoB}$*LC-PEG* was incubated with cells for 4 h, the dendrimer, lipid, and the nanoassembly (yellow spots) were attached on the cell membrane. After 12 h, the lipid was still on the cell membrane while the dendrimer was found inside the cells, suggesting that the nanoassembly dissociated and released the dendrimer. Furthermore, the DOX delivered by the *DLC-PEG* nanoassembly was internalized into cells after 12 h incubation. Notably, dendrimers/DOX (red signal) delivered were not localized in the lysosomes (green signal; Figure 23B), but in the cytosol. This suggests that the dendrimers might not be internalized via the common endocytosis or macropinocytosis pathways. Thus, the effects of temperature and specific pathway inhibitors—chlorpromazine (an inhibitor of the clathrin-dependent pathway[75]), filipin (an inhibitor of the caveolae-dependent pathway[76]) and wortmannin (an inhibitor of the phosphatidylinositol 3-kinasespathway[77])—on the cellular uptake of the nanoassembly were probed using flow cytometry (Figure 23C). The cellular uptake was suppressed to some extent at low temperature (4 °C), suggesting the internalization was mainly energy dependent. The presence of chlorpromazine, filipin, or wortmannin had almost no effect on the cellular uptake

of the dendrimer, indicating that the cellular uptake of the dendrimers in the assembly was not through the common endocytosis or macropinocytosis pathways.

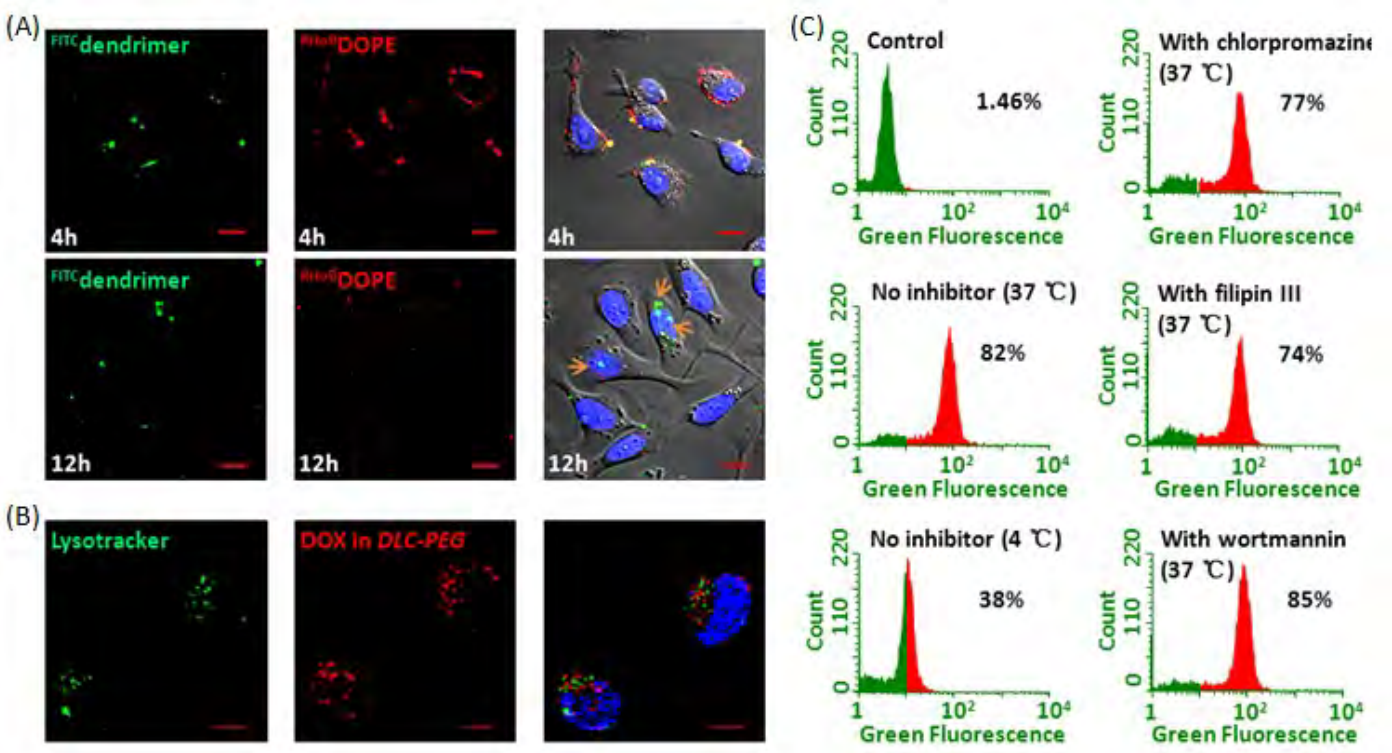


**Figure 23.** Cell interaction and disassociation (A), intracellular localization (B), and internalization (C) of the nanoassembly. A, Cellular uptake of *DLC-PEG* by SKOV-3 cells observed. The cells were treated with dual-labeled $^{FITC}D^{RHoB}$*LC-PEG* nanoassembly for 4 and 12 h, respectively. The FITC-equivalent dose was 60 μg/ml. $^{FITC}$dendrimer is shown in green; $^{RHoB}$DOPE is shown in red; cell nuclei were stained with Draq 5 in blue. All scale bars were 10 μm. B, Subcellular localization of *DLC-PEG*/DOX. The SKOV-3 cells were treated with *DLC-PEG*/DOX at a DOX-equivalent dose of 0.8 μg/ml for 6 h. Lysotracker dyed lysosomes shown in green; DOX loaded in *DLC-PEG* shown in red. All scale bars were 10 μm. C, The FITC-positive SKOV-3 cells after treatment with $^{FITC}$*DLC-PEG* for 6 h at different temperatures or at 37 °C in the presence of chlorpromazine, filipin or wortmannin. The FITC-equivalent dose was 60 μg/ml.

We used a fluorescence-resonance energy-transfer (FRET) approach[78, 79] to probe the fusion of the lipid layer with the cell membrane. Two FRET fluorescent dyes, RHoB and NBD, were separately tethered to the DOPE lipid ($^{RHoB}$DOPE and $^{NBD}$DOPE). They were mixed with DOPE at a DOPE/$^{RHoB}$DOPE/$^{NBD}$DOPE molar ratio of 94/1/5 and used to form the lipid-dually labeled nanoassembly, $D^{RHoB/NBD}$*LC-PEG* (Figure 24A). A FRET efficiency index, *R*, can be calculated from the intensity ratio of $^{RHoB}$DOPE fluorescence at 585 nm to the $^{NBD}$DOPE fluorescence at 525 nm excited at 450 nm[78]. Upon excitation at 450 nm, the intact $D^{RHoB/NBD}$*LC-PEG* nanoassembly had a strong FRET-fluorescence peak at 585 nm and a weak peak at 525 nm with an *R* value of 3.4. As a control experiment, adding 0.24 vol% Triton X-100 to dissolve and dissemble the nanoassembly completely eliminated the FRET. The treated cells, which were treated with $D^{RHoB/NBD}$*LC-PEG* nanoassembly

PBS-CM solution for 6 h and then isolated and resuspended in fresh PBS-CM solution, had a weak FRET with an *R* value of 0.39, indicating the fusion of the lipid layer with the cell membrane.

To test the extracellular dendrimer release, we incubated $^{FITC}$*DLC-PEG* with SKOV-3 cells in PBS-CM solution at 37 °C for different times and then collected the extracellular nanoassembly solutions. The $^{FITC}$dendrimer fluorescence was measured and the nanoassembly integrity was probed again using the AuNP quenching method (Figure 24B). After the nanoassembly was incubated with the cells for 5 min, some $^{FITC}$dendrimer fluorescence became quenchable by AuNPs, and the peak FITC emission shifted from 520 nm to 530 nm, typical for FITC in a hydrophilic environment. This phenomenon became much more pronounced after longer incubation. After 45 min incubation, the $^{FITC}$dendrimer fluorescence could be completely quenched after adding 100 μl of the AuNP solution, which was very similar to that of the free $^{FITC}$dendrimer, indicating that the dendrimers in the extracellular solution were mostly exposed to an aqueous environment.

Therefore, it can be concluded that the fusion of the nanoassembly lipid layer to the cell membrane stripped off its lipid layer and released dendrimers either into the cell cytosol or the extracellular medium. This triggering resolves the size dilemma between blood circulation and tumor penetration.

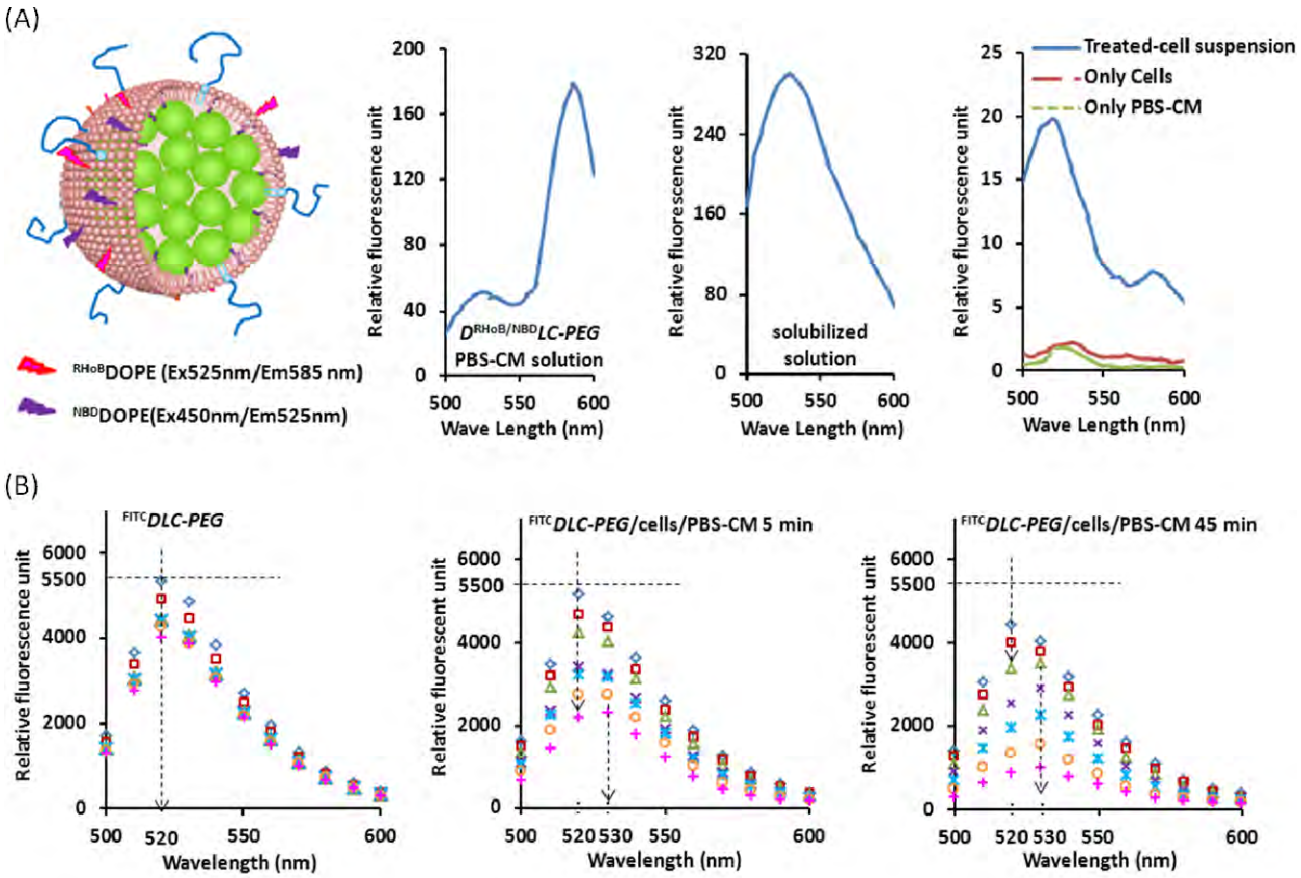


**Figure 24.** The fusion study of the *DLC-PEG* nanoassembly with the cell membrane (A) and its extracellular dendrimer release (B). A, Fusion assay using a fluorescence-resonance energy-transfer (FRET) approach. The *DLC-PEG* lipid layer was dual labeled with $^{NBD}$DOPE (ex 450 nm/em 525 nm) and $^{RHoB}$DOPE (ex 525 nm/em 585 nm) at a DOPE/$^{RHoB}$DOPE/$^{NBD}$DOPE molar ratio of 94/1/5. All the fluorescence emission spectra were recorded excited by a 450 nm laser. B, Dendrimer released into extracellular medium from *DLC-PEG* induced by fusion. The FITC fluorescence of the solution was measured before and after adding different amounts of gold nanoparticles (AuNPs; 1 mg/ml; before quenching, diamond; 10 µl AuNPs, square; 20 µl, triangle; 40 µl, X; 60 µl, asterisk; 80 µl, circle; 100 µl, cross).

### 3.3.3 *In vitro* and *in vivo* administrations of the nanoassembly

The cytotoxicity of DOX loaded in *DLC-PEG* (*DLC-PEG*/DOX) to three cancer cell lines, MDA-MB-468 and BCAP-37 breast cancer cells and SKOV-3 ovarian cancer cells, was slightly lower than that of free DOX. The blank *DLC-PEG* had no cytotoxicity.

The *in vivo* stealth properties of *DLC-PEG* were compared with standard PCL-PEG micelles. Both the nanoassembly's dendrimer and the PCL-PEG (the PCL end) were conjugated with FITC for nonleaching labeling. A hydrophobic fluorescence probe, DiR, was loaded instead of DOX into the $^{FITC}$*DLC-PEG* nanoassembly and the $^{FITC}$PCL-PEG micelles for tracing because the fluorescence wavelengths of DOX and FITC are partially overlapped. The *DLC-PEG*/DiR (45 nm in diameter) was found to have a blood circulation

similar to that of the well-known long-circulating $PCL_{2.5k}$-$PEG_{5k}$/DiR micelles, suggesting that the nanoassembly indeed had good stealth properties (Figure 25A). The biodistribution profile in organs responsible for clearance (liver, spleen, kidneys) showed no statistical difference at 16 h post-injection. However, *DLC-PEG*/DiR accumulated more in SKOV-3 xenografted tumor than $PCL_{2.5k}$-$PEG_{5k}$/DiR as calculated by the overall fluorescence intensity of either FITC labeled carriers or the loaded DiR dye in the tumor cells. The $^{FITC}$dendrimer accumulated in tumor was 1.7 ($p$ = 0.038) times of FITC-labeled $PCL_{2.5k}$-$PEG_{5k}$; similarly, DiR-loaded *DLC-PEG* accumulated in the tumor was 1.5 times of the DiR-loaded $PCL_{2.5k}$-$PEG_{5k}$ (Figure 25B).

The dual-labeled $^{FITC}D^{RHoB}$*LC-PEG* nanoassembly was loaded with a model drug DiR ($^{FITC}D^{RHoB}$*LC-PEG*/DiR) and used to observe the intratumoral distribution, nanoassembly dissociation, and drug release using confocal microscopy. Figure 25C shows a representative part of a solid tumor slice (10 μm thick) excised from SKOV-3 tumor-bearing mice at 16 h post-injection with $^{FITC}D^{RHoB}$*LC-PEG*/DiR. The $^{FITC}$dendrimer (green signal) was separate from the $^{RHoB}$DOPE (red signal), suggesting the dissociation of the dendrimers and lipid layer in the tumor. In Figure 25D, the green signal of the $^{FITC}$dendrimer and the red signal of DiR are mostly overlapped as yellow spots after the nanoassembly extravasated from the blood vessel into the tumor (magnified area 1), and they still overlapped during deep penetration through the tumor tissue (magnified area 2), indicating that the dendrimer retained the DiR well. Furthermore, the dendrimer was distributed throughout the tumor. In contrast, a relatively small number of the 75 nm $PCL_{2.5k}$-$PEG_{5k}$ appeared mostly at the invasive edges and very few appeared inside the tumor, where it released the DiR. This indicates that the nanoassembly could circulate longer in the bloodstream and efficiently accumulat in the tumor. Once in the tumor, the nanoassembly shed the lipid layer and released the dendrimer; the dendrimer carried the loaded drug (DiR here), penetrating and distributing throughout the whole tumor.

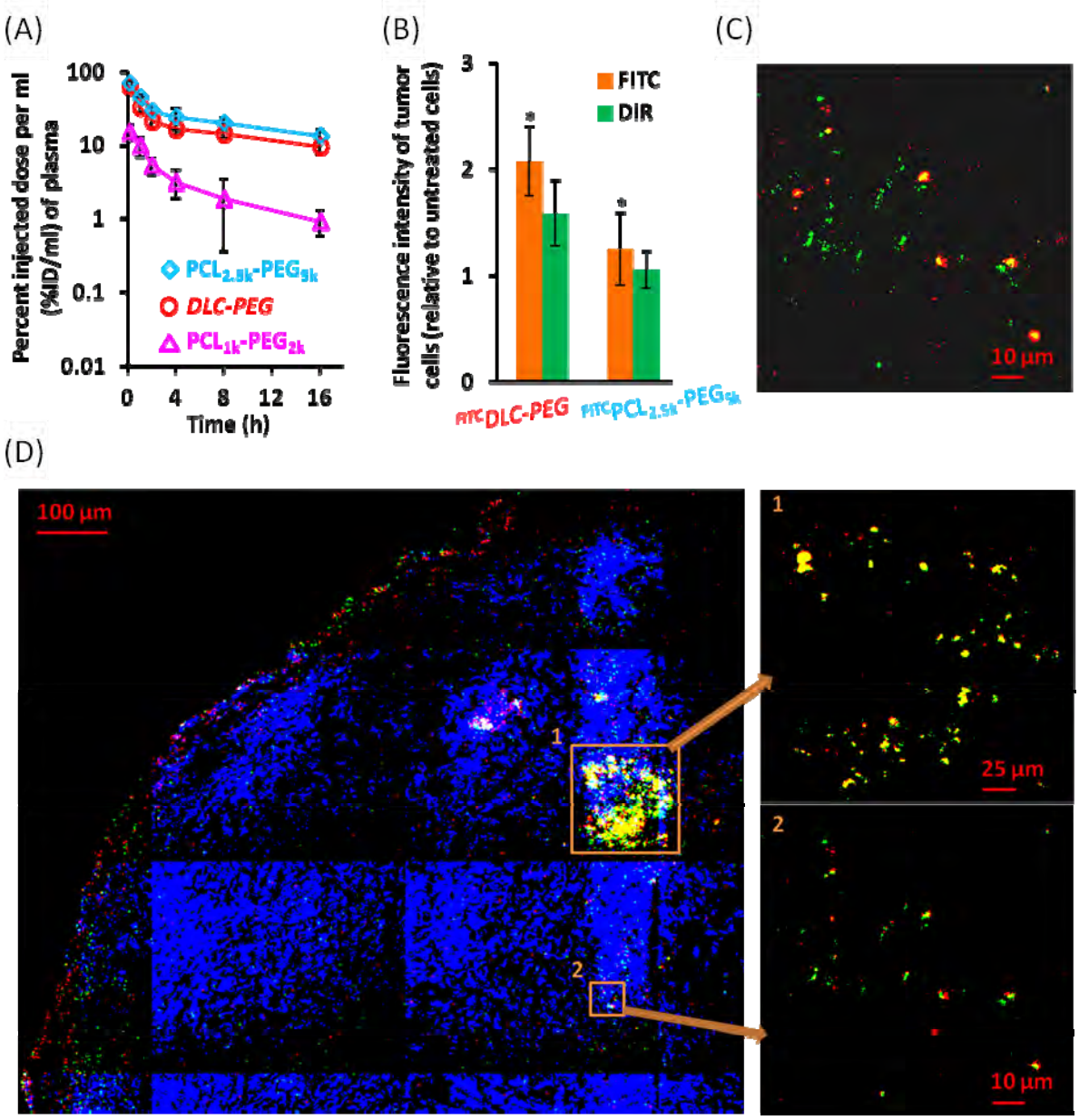


**Figure 25.** *In vivo* blood clearance (A), tumor accumulation (B), disassociation (C), and tumor distribution (D) of *DLC-PEG* nanoassembly. A, Blood clearance of DiR loaded *DLC-PEG* nanoassembly (45 nm in diameter), $PCL_{2.5k}$-$PEG_{5k}$ (75 nm) and $PCL_{1k}$-$PEG_{2k}$ (25 nm) nanoparticles in female athymic mice after a single dose of 0.15 mg DiR/kg body weight. B, The accumulation of DiR-loaded $^{FITC}$*DLC-PEG* nanoassembly and $^{FITC}PCL_{2.5k}$-$PEG_{5k}$ nanoparticles in tumors is calculated in terms of fluorescence intensity of tumor cells. C & D, The dissociation and the intratumoral distribution of DiR-loaded $^{FITC}$dendrimer- and $^{RHoB}$DOPE-labeled nanoassembly ($^{FITC}D^{RHoB}LC$-*PEG*/DiR) in SKOV-3 tumor tissue.

We further examined the tumor accumulation and penetration of the real drug DOX delivered by *DLC-PEG* in BCAP-37 tumor-bearing mice and compared them with similar-sized $PCL_{2k}$-$PEG_{2k}$/DOX nanoparticles (40 nm in diameter). The *DLC-PEG* delivered 1.7 ($p$ = 0.024) times as much DOX as was delivered by $PCL_{2k}$-$PEG_{2k}$ at 16 h post-injection (Figure 26A). The confocal image of a tumor slice (10 μm thick) sectioned from the tumor treated with *DLC-PEG*/DOX clearly had DOX much more homogeneously distributed in the tumor,

whereas the DOX delivered by $PCL_{2k}$-$PEG_{2k}$ was mostly retained in the invasive edge (Figure 26B & C). This further proves that the nanoassembly *DLC-PEG* could release the dendrimers once in the tumor by stripping off the lipid layer, and the small dendrimer could penetrate more deeply into the whole tumor tissue, which is advantageous over conventional fixed-size nanoparticles.

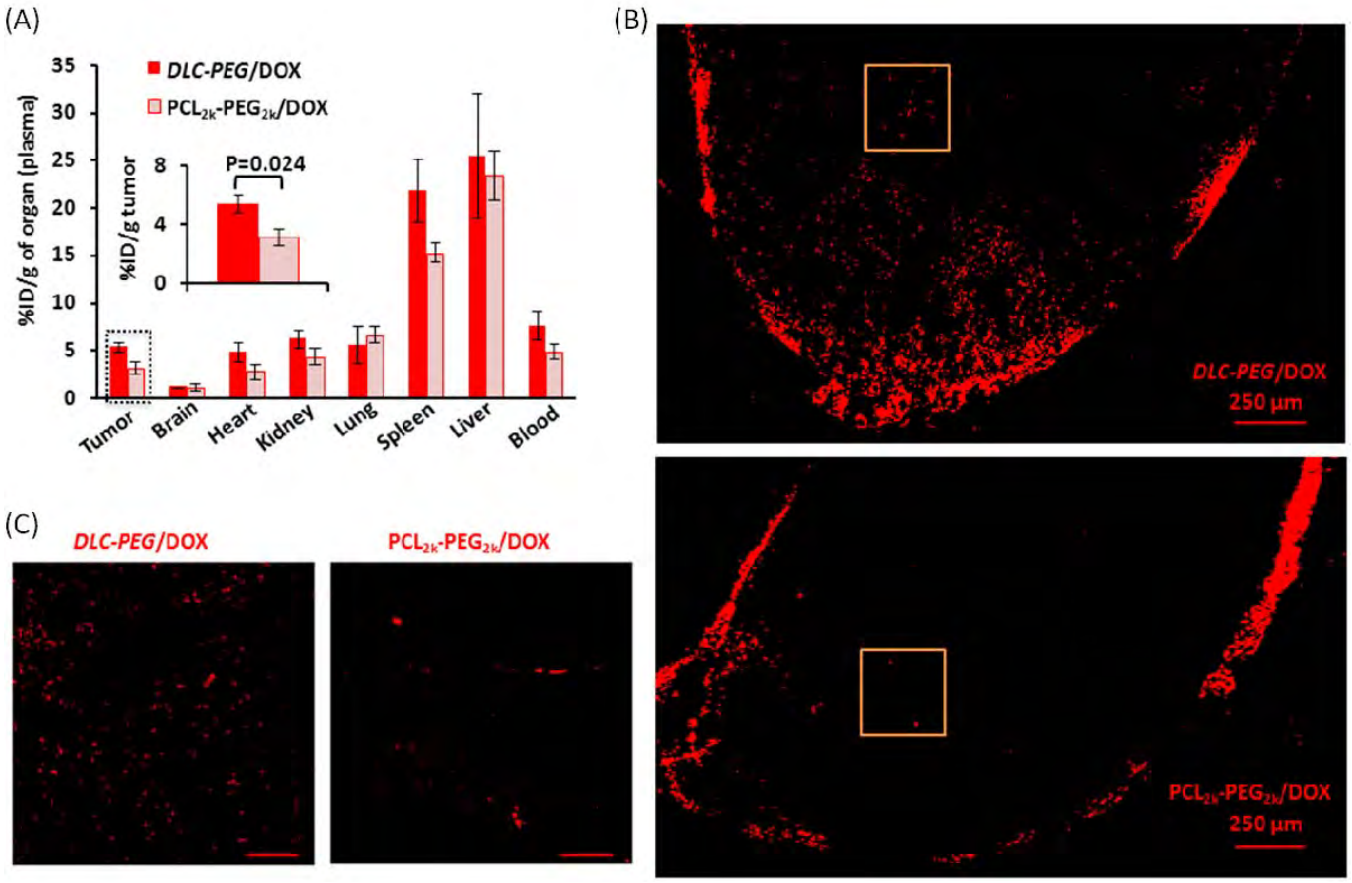


**Figure 26.** DOX Biodistributions and intratumoral distributions of *DLC-PEG*/DOX and its control $PCL_{2k}$-$PEG_{2k}$/DOX. A, Biodistributions of *DLC-PEG*/DOX (45 nm) and $PCL_{2k}$-$PEG_{2k}$/DOX (40 nm) in BCAP-37 tumor-bearing mice 16 h after a single injection of 1 mg DOX/kg body weight. B, The representative confocal images obtained under tile scanning of the complete tumor tissue slides (10 μm thick, a half of the whole slides) sectioned from the BCAP-37 tumors. DOX is shown in red. The magnified views of the selected areas in (B) are shown in C. The scale bar is 50 μm.

### 3.3.4 Conclusion

We have demonstrated that the dendrimer/lipid (*DLC-PEG*) nanoassembly can improve tumor accumulation, penetration, and cellular uptake. The nanoassembly behaves like a “cluster bomb”: it circulates in the blood compartment for a long period, efficiently accumulates in a tumor, and subsequently sheds off the lipid layer to release the small dendrimers carrying drugs (bomblets) to penetrate the tight tumor tissue. The released pH-sensitive dendrimers shepherded the drugs past the multidrug resistance and were quickly

internalized by the cells. The “cluster bomb” concept may be a very promising approach uniting the needed properties for high chemotherapeutic efficacy.

## 4. Novel nanorods as carriers for drug delivery

Prolonging the nanocarrier’s blood circulation time increases its opportunity to pass through the leaky vasculature, and thereby its extravagation into the tumor tissue[80]. Surface properties and size of a nanocarrier are the two important factors affecting its blood circulation time[81-85]. Besides, the nanocarrier shape has been recognized as another important parameter strongly affecting its circulation time[86-91]. PEGylated metallic and inorganic nanorods[92, 93] as models were demonstrated to long circulate like wormlike micelles[86-88] and have the ability to penetrate tumor efficiently via the enhanced pore transportation[94] and fast cellular uptake[95-97] compared to nanospheres; however, they cannot be used in clinics for intravenous drug delivery. Unfortunately, amphiphilic copolymers form rod-like morphology only within very narrow composition ranges depending on the polymer natures[98, 99]

Herein, we reported a self-assembly of well-defined linear-dendritic conjugates, PEG–*block*-dendritic polylysine-camptothecin (PEG-xCPT), into rod-like nanocarriers characteristic of biodegradability, high drug loading contents free of burst release, long blood circulating, fast cellular internalization, and intracellular drug release (Figure 27).

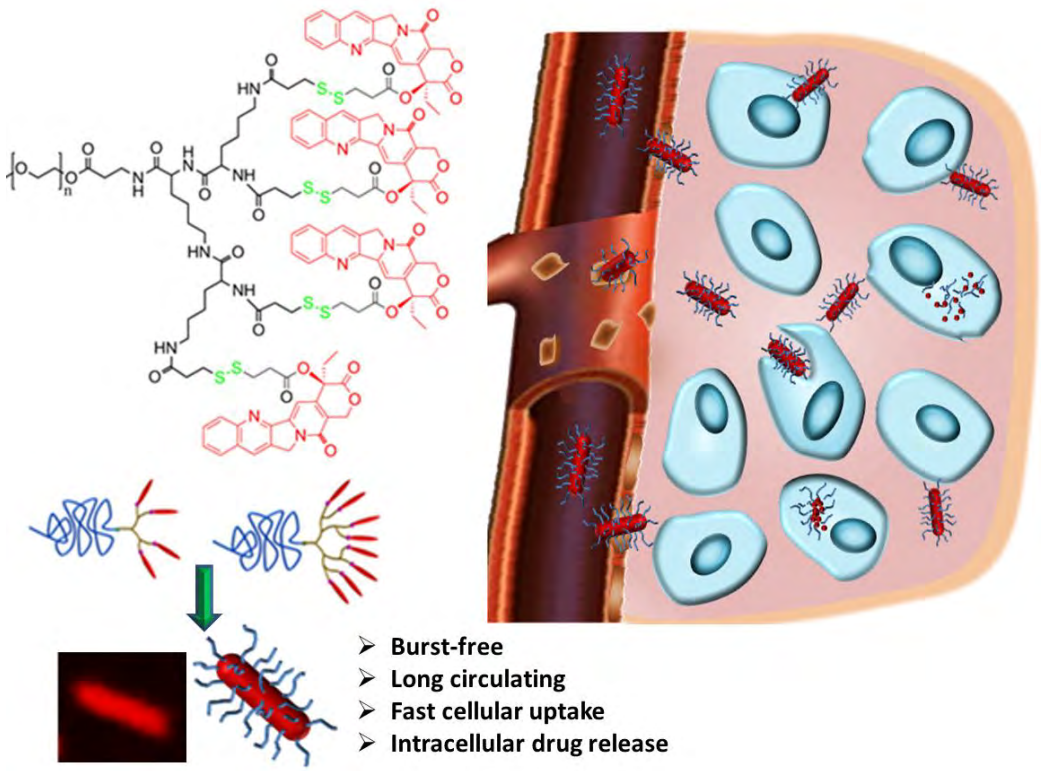


**Figure 27.** Self-assembly of $PEG_{45}$-dendritic polylysine-camptothecin (PEG-xCPT) conjugates into biodegradable nanospheres or nanorods with high drug loading: The formation of the morphologies was determined by the generation of the dendritic polylysine and the number of the conjugated CPT. Nanorods with short length (< 500 nm) have characteristics of long blood circulating, fast cellular internalization, and intracellular drug release.

**4.1 Nanorod preparation**

The CPT-PDP containing a disulfide bond and an *NHS* active ester group was first synthesized. PEG-*block*-dendritc PLL (DPLL) of different generations was prepared and then reacted with a corresponding amount of CPT-PDP to obtain PEG-DPLL conjugated with 1, 2, 4 or 8 CPT molecules. The structures of the conjugates PEG-xCPT were characterized by MALDI-TOF MS spectra, $^1$H NMR spectra, HPLC and GPC. Notably, the CPT contents of $PEG_{45}$-CPT, $PEG_{45}$-DiCPT, $PEG_{45}$-TetraCPT and $PEG_{45}$-OctaCPT were 13.4%, 21.4%, 30.6% and 38.9% by weight, respectively.

The PEG-xCPT formed nanoparticles at concentrations higher than their CMCs. The morphologies of the nanoparticles in the aqueous solution were observed using TEM (Figure 28 A-C). $PEG_{45}$-CPT and $PEG_{45}$-DiCPT (Figure 28 A) formed uniform ~100 nm nanospheres. Interestingly, $PEG_{45}$-TetraCPT and $PEG_{45}$-OctaCPT formed unusual nanorods (Figure 28B & C). The nanorods of $PEG_{45}$-TetraCPT were about 60 nm in diameter and 500 nm long, and those of $PEG_{45}$-OctaCPT were about 100 nm in diameter and about one

micrometer long. These structures were further confirmed by confocal fluorescence microscopy after loaded with a fluorescent dye nile red (Figure 28D-E).

The stability study of the nanostructures showed the $PEG_{45}$-DiCPT nanospheres and $PEG_{45}$-TetraCPT nanorods were stable over 5 days and their sizes did not change over the time, while $PEG_{45}$-OctaCPT nanorods slightly aggregated. All these nanospheres or nanorods did not release any CPT in PBS at 37 °C. However, in the presence of DTT, the nanospheres or nanorods immediately released CPT-SH as detected by HPLC.

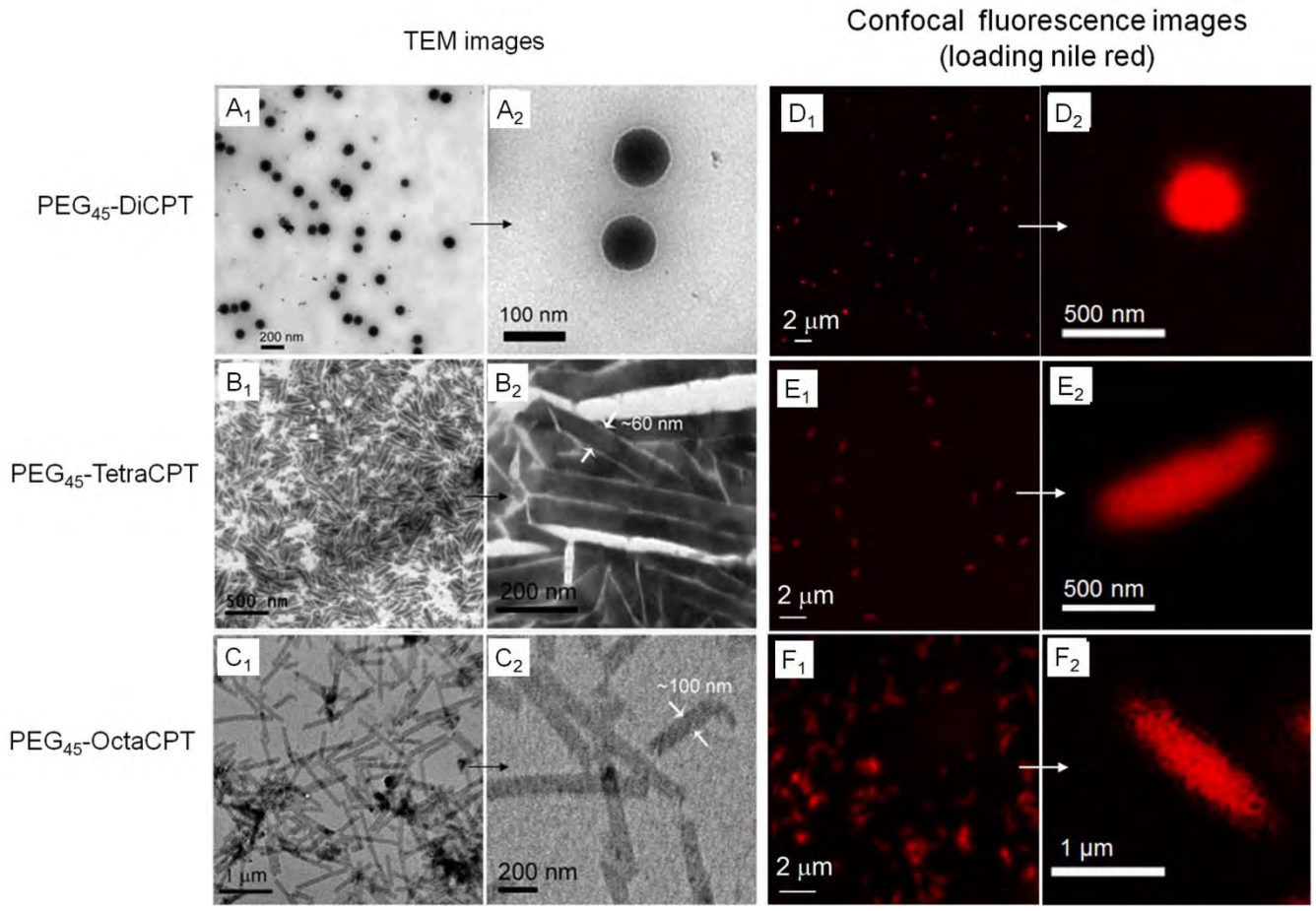


**Figure 28.** The TEM images of $PEG_{45}$-DiCPT (A), $PEG_{45}$-TetraCPT (B), $PEG_{45}$-OctaCPT (C) nanostructures and the confocal florescence images of $PEG_{45}$-DiCPT (D), $PEG_{45}$-TetraCPT (E) and $PEG_{45}$-OctaCPT (F) nanostructures loaded with Nile red and their corresponding enlarged images.

**4.2 Drug delivery by the nanorod**

DOX was loaded as a tracer to the nanocarriers ($PEG_{45}$-DiCPT/DOX) and nanorods ($PEG_{45}$-TetraCPT/DOX and $PEG_{45}$-OctaCPT/DOX) for cell internalization study using confocal microscopy and flow cytometry (Figure 29). As shown in Figure 29A, the cellular uptakes of DOX-loaded nanospheres or nanorods were different from that of free DOX. Free DOX easily entered the non-drug-resistant cells (MCF-7) by passive

diffusion, as evidenced by the strong fluorescence in whole cells; only very weak DOX fluorescence was observed in multidrug-resistant cells (MCF-7/ADR) since DOX is a substrate of their drug resistance. In contrast, strong DOX fluorescence was observed in both MCF-7 and MCF-7/ADR cells after they were cultured with DOX-loaded nanoparticles for one hour, and the intracellular fluorescent intensity increased gradually with prolonging the culturing time (4 or 8 h). Two more phenomena were further observed: In MCF-7 cells, the intracellular DOX distributed in the whole cells after 8 h culture, including the nuclei; but in MCF-7/ADR cells, the intracellular DOX could not enter the nuclei. Furthermore, the DOX-intensity of the cells cultured with the nanorods ($PEG_{45}$-TetraCPT/DOX and $PEG_{45}$-OctaCPT/DOX) was much higher than those cultured with the nanospheres ($PEG_{45}$-DiCPT/DOX), particularly those with the $PEG_{45}$-OctaCPT/DOX nanorods, suggesting much faster cellular uptake of the nanorods than that of the nanospheres. This was further proven by quantitation using by flow cytometry (Figure 29B) in terms of the fold increase of the mean fluorescence intensity relative to control. Clearly, at each time points, the cells cultured with nanorods $PEG_{45}$-TetraCPT/DOX or $PEG_{45}$-OctaCPT/DOX had higher fluorescent intensities than that of those cultured with the spherical $PEG_{45}$-DiCPT/DOX (all $p<0.01$). At 8 h culture, the DOX intensity of the cells cultured with $PEG_{45}$-TetraCPT/DOX or $PEG_{45}$-OctaCPT/DOX was 1.15 or 1.39 fold of those cultured with $PEG_{45}$-DiCPT/DOX.

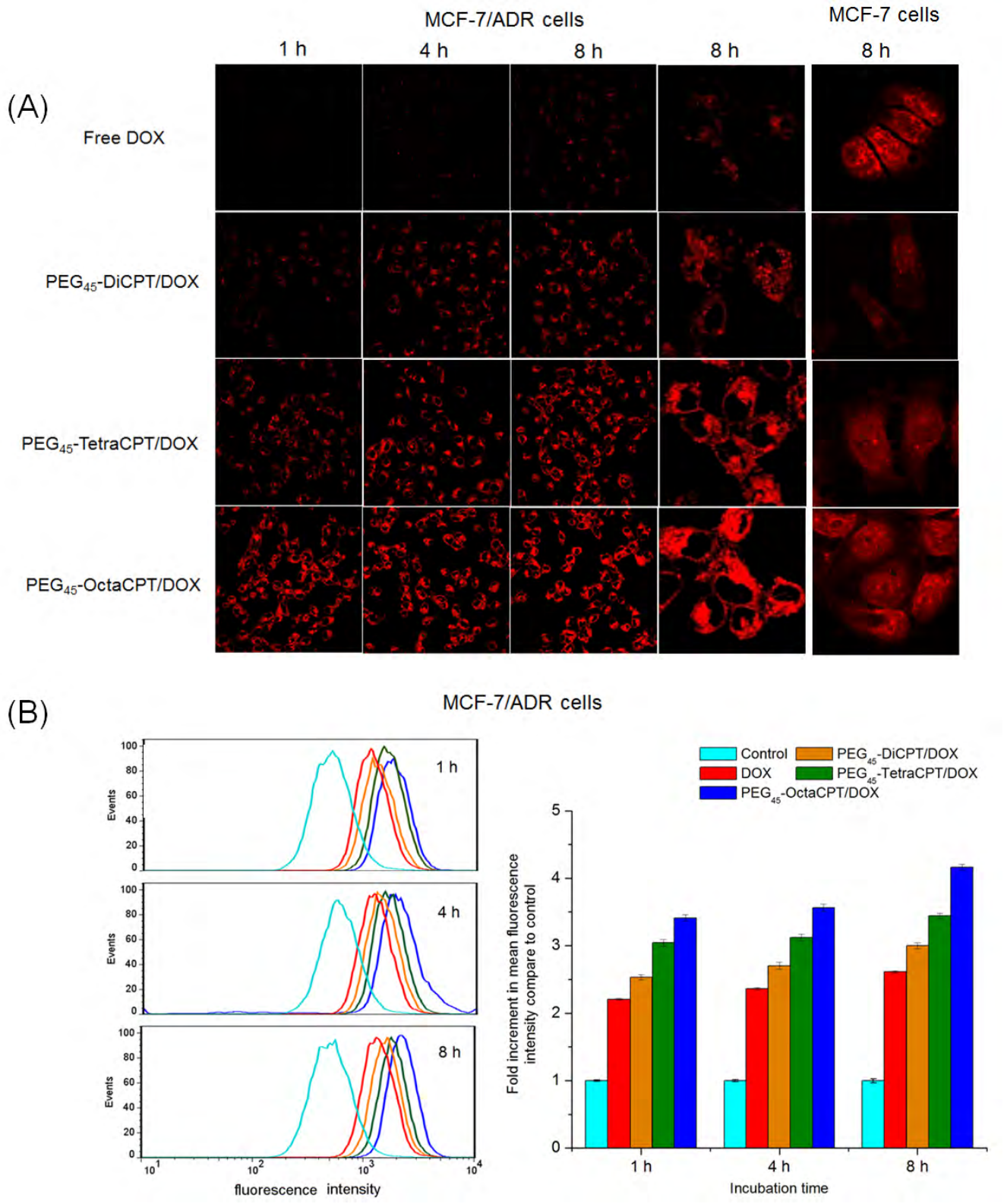


**Figure 29.** Cellular uptake study of free DOX, $PEG_{45}$-DiCPT/DOX, $PEG_{45}$-TetraCPT/DOX and $PEG_{45}$-OctaCPT/DOX by confocal microscopy (A) and flow cytometry (B). The free DOX and the DOX-loaded nanostructures (DOX dose: 4 μg/mL) were cultured individually with MCF-7 or MCF-7/ADR cancer cells at 37 $^{o}$C for 1, 4 or 8 hours.

**4.3 In vitro and in vivo administrations of the nanorod**

The cytotoxicity of free CPT, and the nanospheres/nanorods to MCF-7 or MCF-7/ADR cancer cells was evaluated using the MTT assay. With 72 h culture, the $IC_{50}$ value to MCF-7 cells was 0.138 μg/mL for $PEG_{45}$-DiCPT, 0.073 μg/mL for $PEG_{45}$-TetraCPT and 0.070 μg/mL for $PEG_{45}$-OctaCPT, higher than that of CPT.

The pharmacokinetics and biodistribution of nanospheres and nanorods were studied after *iv* administration to BALB/c mice. Less than 1% of the injected free CPT was reported to remain in the blood after 30 min[100]. The nanospheres or nanorods had much prolonged blood circulation times than CPT, but $PEG_{45}$-TetraCPT nanorods had the longest blood circulation time. Thus, $PEG_{45}$-TetraCPT nanorods had a much better stealth property than the $PEG_{45}$-DiCPT nanospheres, suggesting that nanorods more effectively resisted opsonization or nonspecific binding of proteins. The biodistributions of the nanocarriers in terms of CPT concentration in different organs of mice at 4 and 24 h post *iv* administration were evaluated. At 4 h, spleen was the major organ sequestering the nanocarriers for all three systems. Thus, the spleen was still responsible for the clearance of the nanospheres and nanorods. $PEG_{45}$-TetraCPT had lower concentrations in liver and spleen than $PEG_{45}$-DiCPT. After 24 h, $PEG_{45}$-DiCPT almost disappeared from all the organs. $PEG_{45}$-TetraCPT was still found in the spleen (22.05 ± 6.33% ID/g tissue) and blood (3.59 ± 0.29 % ID/g blood).

Ex vivo imaging of excised tissues and tumors at 8 h post-injection showed an obvious tumor accumulation of the DOX-loaded nanoparticles (Figure 30). The mice injected with $PEG_{45}$-DiCPT/DOX or $PEG_{45}$-OctaCPT/DOX had higher DOX fluorescence in liver than that injected with $PEG_{45}$-TetraCPT/DOX. The mouse injected with $PEG_{45}$-OctaCPT/DOX had higher DOX fluorescence in lung than those injected with other nanoparticles. Very low fluorescence was observed in heart and spleen for all the mice. Side-by-side comparison of the tumors from mice injected with $PEG_{45}$-DiCPT/DOX or $PEG_{45}$-TetraCPT/DOX is shown in Figure 30C. Fluorescence intensity in tumors of the mice injected with $PEG_{45}$-TetraCPT/DOX was 2.8 times of those injected with $PEG_{45}$-DiCPT/DOX. The t-student test indicated the DOX fluorescence in the tumors from mice injected with nanospheres and nanorods was statistically different.

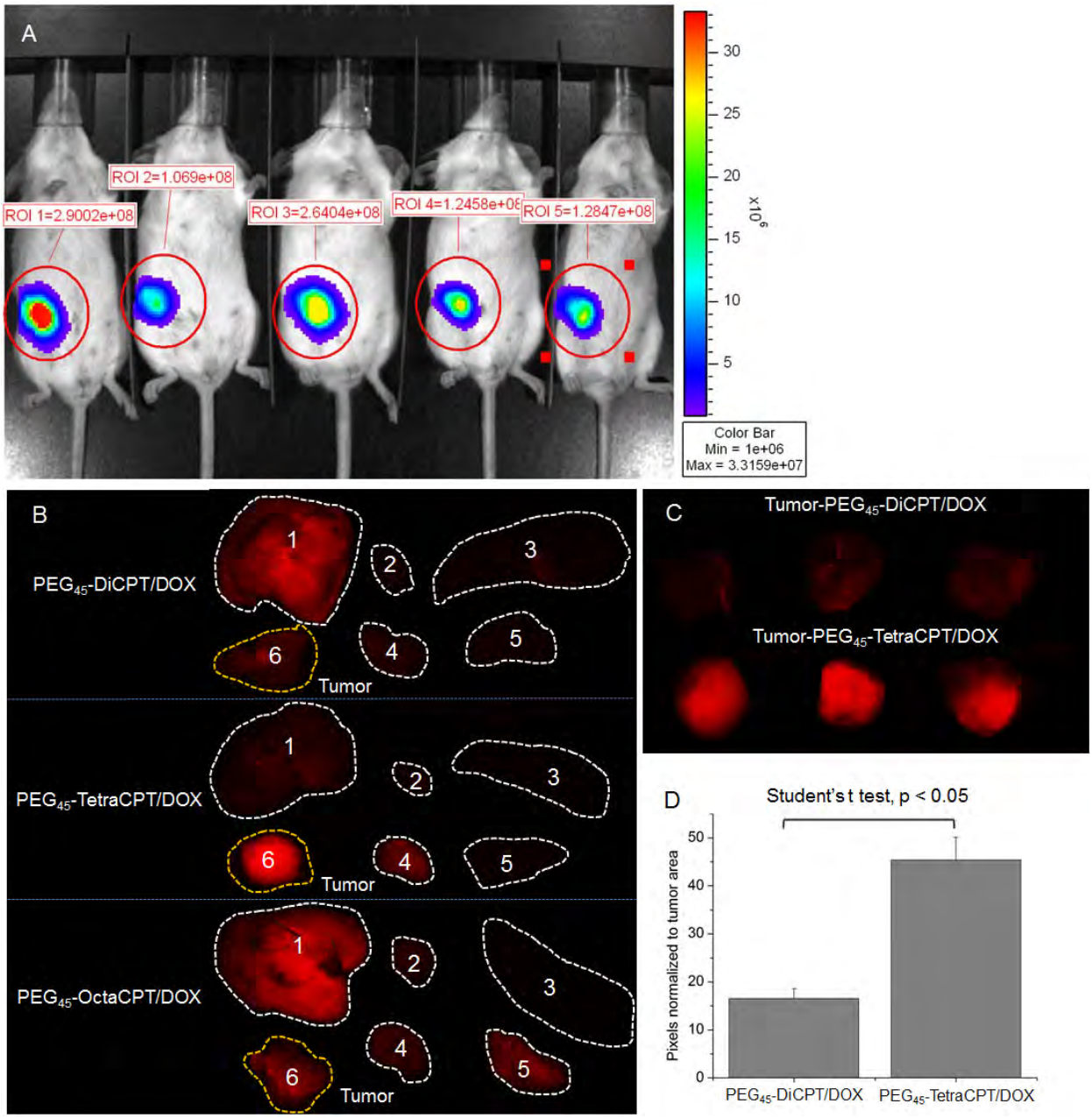


**Figure 30**. (A) Bioluminescence images showing mice bearing 4T1-Luc breast tumor in mammary fat pad two weeks after implant. Mice were intraperitoneal injected with D-luciferin (150 mg/kg body weight) 10 min before imaging with Xenogen IVIS Lumina system. (B) Mice bearing 4T1-Luc breast tumor were intravenously injected with DOX-loaded nanoparticles (5 mg DOX-equivalent/kg body weight). After 8 h, the mice were sacrificed and the tumors and various organs (1. Liver, 2. Heart, 3. Spleen, 4. Kidney, 5. Lung, 6. Tumor) were imaged with the Maestro FLEX *In Vivo* Imaging System. (C) Tumors of mice injected with $PEG_{45}$-DiCPT/DOX or $PEG_{45}$-TetraCPT/DOX were imaged side by side with the Maestro FLEX *In Vivo* Imaging System and (D) the pixels normalized to tumor area analyzed with Maestro software.

### 4.4 Conclusion

We demonstrated a facile approach to fabricate polymer-drug conjugate nanorods for cancer-drug delivery. Using a hydrophobic drug as the hydrophobic moiety, well-defined amphiphilic linear-dendritic drug

conjugates, PEG-b-dendritic polylysine-CPT, were synthesized. Tailoring their generation and the number of the conjugated CPT molecules induced the linear-dendritic conjugates to self-assemble into spherical or rod-like nanostructures stable at the physiological conditions but quickly releasing the drug CPT once in the cytosol. The shape of the nanostructures affected their cellular uptake and in vivo blood clearance. The nanorods were taken up more efficiently by cancer cells than nanospheres. The nanorods with medium lengths (<500 nm) also had a much better stealth property and thus a much longer blood circulation time than the nanospheres.

## 5. Review of translational nanocarriers for drug delivery

Design of nanocarriers with more efficient drug delivery and thus to achieve higher therapeutic efficacy is a pressing need due to the current cancer drug delivery has only achieved modest therapeutic benefits[101, 102]. Therefore, we proposed a truly translational nanocarrier should firstly capable of simultaneously satisfying *2R2S* requirements, which is "drug *R*etention in blood circulation *vs. R*elease in tumor cells (*2R*)" and "surface *S*tealthy in blood circulation and tumor tissues vs. *S*ticky to tumor cells (*2S*)", to delivery drugs specifically at the right time and the right place[103]. Furthermore, while the 2*R*2*S* capability of a nanocarrier may render its resulting nanomedicine efficacy and safety potential for clinical translation, other two elements, the feasibility of the nanocarrier materials to be proved for use as excipients (referred to as material excipientability) and the ability to establish scaling up production processes for good manufacture processes (GMP) for the nanocarrier and its formulation with drug (nanomedicine) (referred to as process scale-up ability) are also indispensible for the nanomedicine truly translational from the benchtop to the bedside (Figure 31)[103]. The challenge to develop truly translational nanocarriers and nanomedicine is to use less excipientable materials and simple processes of scale-up ability to produce nanocarriers with optimal *2R2S* capability. While the research aimed at proof of concepts remains important, it is important to increasingly focus on comprehensive approaches or systems that include *all* the three key elements, as early as possible in the innovation chain to speed up developments of translational nanomedicine.

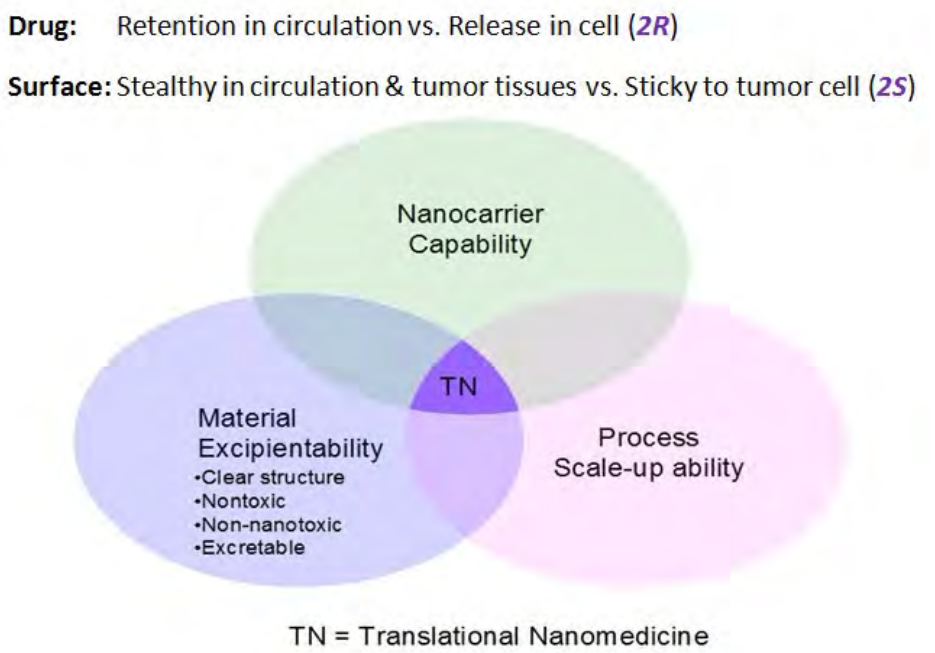


**Figure 31.** The three elements for translational nanomedicine: the nanocarrier should have the 2*R*2*S* capability and its material should be suitable for excipient use (referred to as material excipientability); the production of the nanocarrier and its formulation with drug (nanomedicine) should be able to scale up for good manufacture process (GMP) (scale-up ability).

## 6. References


1. Fojo, T.; Coley, H. M. *Clin. Breast Cancer* **2007,** 7, (10), 749-756.
2. Robey, R. W.; Polgar, O.; Deeken, J.; To, K. W.; Bates, S. E. *Cancer Metast. Rev.* **2007,** 26, (1), 39-57.
3. Chang, X.B. *Cancer Metast. Rev.* **2007,** 26, (1), 15-37.
4. Hirota, T.; Takane, H.; Higuchi, S.; Ieiri, I. *Curr. Drug Metab.* **2008,** 9, (1), 34-38.
5. Duvvuri, M.; Krise, J. P. *Front. Biosci.* **2005,** 10, 1499-1509.
6. Manzoor Ashley, A.; Lindner Lars, H.; Landon Chelsea, D.; Park, J.Y.; Simnick Andrew, J.; Dreher Matthew, R.; Das, S.; Hanna, G.; Park, W.; Chilkoti, A.; Koning Gerben, A.; Ten Hagen Timo, L. M.; Needham, D.; Dewhirst Mark, W. *Cancer Res.* **2012**, 72, (21), 5566-5575.
7. Zhu, L.; Kate, P.; Torchilin, V. P. *ACS Nano* **2012,** 6, (4), 3491-3498.
8. Pichon, C.; Goncalves, C.; Midoux, P. *Adv. Drug Deliver. Rev.* **2001,** 53, (1), 75-94.
9. Cho, Y. W.; Kim, J. D.; Park, K. *J. Pharm. Pharmacol.* **2003,** 55, (6), 721-734.
10. Yang, S. R.; Lee, H. J.; Kim, J. D. *J. Control. Release* **2006,** 114, (1), 60-68.
11. Xu, P.; Van Kirk, E.; Zhan, Y.; Murdoch, W. J.; Radosz, M.; Shen, Y. *Angew. Chem. Int. Ed* **2007,** 46, 4999-5002.
12. Zhou, Z.; Shen, Y.; Tang, J.; Fan, M.; Van Kirk, E. A.; Murdoch, W. J.; Radosz, M. *Adv. Funct. Mater.* **2009,** 19, (22), 3580-3589.
13. Akinc, A.; Thomas, M.; Klibanov, A. M.; Langer, R. *J. Gene Med.* **2005,** 7, (5), 657-663.
14. Lee, E. S.; Shin, H. J.; Na, K.; Bae, Y. H. *J. Control. Release* **2003,** 90, (3), 363-374.
15. Jordan, R.; West, N.; Ulman, A.; Chou, Y.-M.; Nuyken, O. *Macromolecules* **2001,** 34, (6), 1606-1611.
16. Murthy, N.; Robichaud, J. R.; Tirrell, D. A.; Stayton, P. S.; Hoffman, A. S. *J. Control. Release* **1999,** 61, (1-2), 137-143.
17. Guin, S.; Yao, H.P.; Wang, M.H. *Mol. Pharm.* **2010,** 7, (2), 386-397.
18. Jung, S. H.; Jung, S. H.; Seong, H.; Cho, S. H.; Jeong, K.S.; Shin, B. C. *Int. J. Pharm.* **2009,** 382, (1-2), 254-261.
19. Tekade, R. K.; Kumar, P. V.; Jain, N. K. *Chem. Rev. (Washington)* **2009,** 109, (1), 49-87.
20. Astruc, D.; Boisselier, E.; Ornelas, C. *Chem. Rev. (Washington)* **2010,** 110, (4), 1857-1959.

21. Jang, W.D.; Kamruzzaman Selim, K. M.; Lee, C.H.; Kang, I.K. *Prog. Polym. Sci.* **2009,** 34, (1), 1-23.
22. Sadekar, S.; Ghandehari, H. *Adv. Drug Deliver.Rev.* **2012,** 64, (6), 571-588.
23. Mishra, V.; Gupta, U.; Jain, N. K. *J. Biomater. Sci., Polym. Ed.* **2009,** 20, (2), 141-166.
24. Malik, N.; Wiwattanapatapee, R.; Klopsch, R.; Lorenz, K.; Frey, H.; Weener, J. W.; Meijer, E. W.; Paulus, W.; Duncan, R. *J. Control. Release* **2000,** 65, (1-2), 133-148.
25. Padilla De Jesus, O. L.; Ihre, H. R.; Gagne, L.; Frechet, J. M. J.; Szoka, F. C., Jr. *Bioconjugate Chem.* **2002,** 13, (3), 453-461.
26. Feliu, N.; Walter, M. V.; Montanez, M. I.; Kunzmann, A.; Hult, A.; Nystrom, A.; Malkoch, M.; Fadeel, B. *Biomaterials* **2012,** 33, (7), 1970-1981.
27. Lee, C. C.; MacKay, J. A.; Frechet, J. M. J.; Szoka, F. C. *Nat. Biotechnol.* **2005,** 23, (12), 1517-1526.
28. Gillies, E. R.; Dy, E.; Frechet, J. M. J.; Szoka, F. C. *Mol. Pharm.* **2005,** 2, (2), 129-138.
29. Almutairi, A.; Akers, W. J.; Berezin, M. Y.; Achilefu, S.; Frechet, J. M. J. *Mol. Pharm.* **2008,** 5, (6), 1103-1110.
30. Guillaudeu, S. J.; Fox, M. E.; Haidar, Y. M.; Dy, E. E.; Szoka, F. C.; Frechet, J. M. J. *Bioconjugate Chem.* **2008,** 19, (2), 461-469.
31. Ye, M. Z.; Qian, Y.; Shen, Y. Q.; Hu, H. J.; Sui, M. H.; Tang, J. B. *J. Mater. Chem* **2012,** 22, (29), 14369-14377.
32. Ihre, H.; Hult, A.; Soderlind, E. *J. Am. Chem. Soc.* **1996,** 118, (27), 6388-6395.
33. Ihre, H.; Hult, A.; Frechet, J. M. J.; Gitsov, I. *Macromolecules* **1998,** 31, (13), 4061-4068.
34. Ropponen, J.; Tuuttila, T.; Lahtinen, M.; Nummelin, S.; Rissanen, K. *J. Polym. Sci. Pol. Chem.* **2004,** 42, (22), 5574-5586.
35. Malkoch, M.; Malmstroem, E.; Hult, A. *Macromolecules* **2002,** 35, (22), 8307-8314.
36. Frechet, J. M. J.; Ihre, H.; De Jesus, O. L. P. *J. Am. Chem. Soc.* **2001,** 123, (25), 5908-5917.
37. Parrott, M. C.; Marchington, E. B.; Valliant, J. F.; Adronov, A. *J. Am. Chem. Soc.* **2005,** 127, (34), 12081-12089.
38. Ma, X.; Zhou, Z.; Jin, E.; Sun, Q.; Zhang, B.; Tang, J.; Shen, Y. *Macromolecules* **2013,** 46, (1), 37-42.
39. Ropponen, J.; Nummelin, S.; Rissanen, K. *Org. Lett.* **2004,** 6, (15), 2495-2497.
40. Jin, R.; Dijkstra, P. J.; Feijen, J. *J. Control. Release* **2010,** 148, (1), e41-e43.
41. Dondoni, A.; Marra, A. *Chem. Soc. Rev.* **2012,** 41, (2), 573-586.
42. Wang, N.; Dong, A.; Tang, H.; Van Kirk, E. A.; Johnson, P. A.; Murdoch, W. J.; Radosz, M.; Shen, Y. *Macromol. Biosci.* **2007,** 7, (11), 1187-1198.
43. Lowe, A. B.; Hoyle, C. E.; Bowman, C. N. *J. Mater. Chem.* **2010,** 20, (23), 4745-4750.
44. Syrett, J. A.; Jones, M. W.; Haddleton, D. M. *Chem. Commun. (Cambridge)* **2010,** 46, (38), 7181-7183.
45. Menjoge, A. R.; Kannan, R. M.; Tomalia, D. A. *Drug Discov. Today* **2010,** 15, (5-6), 171-185.
46. Wolinsky, J. B.; Grinstaff, M. W. *Adv. Drug Deliv. Rev.* **2008,** 60, (9), 1037-1055.
47. Shen, Y.; Zhuo, Z.; Sui, M.; Tang, J.; Xu, P.; Van Kirk, E. A.; Murdoch, W. J.; Fan, M.; Radosz, M. *Nanomedicine* **2010,** 5, (8), 1205-1217.
48. Ye, L.; Letchford, K.; Heller, M.; Liggins, R.; Guan, D.; Kizhakkedathu, J. N.; Brooks, D. E.; Jackson, J. K.; Burt, H. M. *Biomacromolecules* **2011,** 12, (1), 145-155.
49. Duncan, R.; Izzo, L. *Adv. Drug Deliv. Rev.* **2005,** 57, (15), 2215-2237.
50. Patri, A. K.; Kukowska-Latallo, J. F.; Baker, J. R. *Adv. Drug Deliv. Rev.* **2005,** 57, (15), 2203-2214.
51. Barenholz, Y. *J. Control. Release* **2012,** 160, (2), 117-134.
52. Gaucher, G.; Marchessault, R. H.; Leroux, J.C. *J. Control. Release* **2010,** 143, (1), 2-12.
53. Jang, S. H.; Wientjes, M. G.; Lu, D.; Au, J. L. S. *Pharm. Res.* **2003,** 20, (9), 1337-1350.
54. Jain, R. K. *Science* **2005,** 307, (5706), 58-62.
55. Jain, R. K. *Adv. Drug Deliv. Rev.* **2001,** 46, (1-3), 149-168.
56. Choi, J.; Credit, K.; Henderson, K.; Deverkadra, R.; He, Z.; Wiig, H.; Vanpelt, H.; Flessner, M. F. *Clin. Cancer Res.* **2006,** 12, (6), 1906-1912.
57. Boucher, Y.; Baxter, L. T.; Jain, R. K. *Cancer Res.* **1990,** 50, (15), 4478-4484.
58. Heldin, C. H.; Rubin, K.; Pietras, K.; Ostman, A. *Nat. Rev. Cancer* **2004,** 4, (10), 806-813.
59. Cabral, H.; Matsumoto, Y.; Mizuno, K.; Chen, Q.; Murakami, M.; Kimura, M.; Terada, Y.; Kano, M. R.; Miyazono, K.; Uesaka, M.; Nishiyama, N.; Kataoka, K. *Nat. Nanotechnol.* **2011,** 6, (12), 815-823.

60. Jain, R. K. *Cancer Res.* **1990,** 50, (3), S814-S819.
61. Holback, H.; Yeo, Y. *Pharm. Res.* **2011,** 28, (8), 1819-1830.
62. Perrault, S. D.; Walkey, C.; Jennings, T.; Fischer, H. C.; Chan, W. C. W. *Nano Lett.* **2009,** 9, (5), 1909-1915.
63. Li, S.D.; Huang, L. *Mol. Pharm.* **2008,** 5, (4), 496-504.
64. Amrite, A. C.; Edelhauser, H. F.; Singh, S. R.; Kompella, U. B. *Mol. Vis.* **2008,** 14, (19-23).
65. Yang, Z.; Leon, J.; Martin, M.; Harder, J. W.; Zhang, R.; Liang, D.; Lu, W.; Tian, M.; Gelovani, J. G.; Qiao, A.; Li, C. *Nanotechnology* **2009,** 20, (16), 165101-165110.
66. Mishra, S.; Webster, P.; Davis, M. E. *Eur. J. Cell Biol.* **2004,** 83, (3), 97-111.
67. Juweid, M.; Neumann, R.; Paik, C.; Perezbacete, M. J.; Sato, J.; Vanosdol, W.; Weinstein, J. N. *Cancer Res.* **1992,** 52, (19), 5144-5153.
68. Ma, X. P.; Tang, J. B.; Shen, Y. Q.; Fan, M. H.; Tang, H. D.; Radosz, M. *J. Am. Chem. Soc.* **2009,** 131, (41), 14795-14803.
69. Shen, Y.; Ma, X.; Zhang, B.; Zhou, Z.; Sun, Q.; Jin, E.; Sui, M.; Tang, J.; Wang, J.; Fan, M. *Chemistry (Weinheim an der Bergstrasse, Germany)* **2011,** 17, (19), 5319-5326.
70. Hatakeyama, H.; Akita, H.; Harashima, H. *Adv. Drug Deliv. Rev.* **2011,** 63, (3), 152-160.
71. Pasut, G.; Veronese, F. M. *Adv. Drug Deliv. Rev.* **2009,** 61, (13), 1177-1188.
72. Rodrigues, D. G.; Maria, D. A.; Fernandes, D. C.; Valduga, C. J.; Couto, R. D.; Ibanez, O. C. M.; Maranhao, R. C. *Cancer Chemother. Pharmacol.* **2005,** 55, (6), 565-576.
73. Kirby, C.; Clarke, J.; Gregoriadis, G. *Biochem. J.* **1980,** 186, (2), 591-598.
74. Cauda, V.; Schlossbauer, A.; Kecht, J.; Zurner, A.; Bein, T. *J. Am. Chem. Soc.* **2009,** 131, (32), 11361-11370.
75. Diaz-Moscoso, A.; Vercauteren, D.; Rejman, J.; Benito, J. M.; Ortiz Mellet, C.; De Smedt, S. C.; Garcia Fernandez, J. M. *J. Control. Release* **2010,** 143, (3), 318-325.
76. Orlandi, P. A.; Fishman, P. H. *J. Cell Biol.* **1998,** 141, (4), 905-915.
77. Davol, P. A.; Bizuneh, A.; Frackelton, A. R. *Anticancer Res.* **1999,** 19, (3A), 1705-1713.
78. Kono, K.; Igawa, T.; Takagishi, T. *Biochim. Biophys. Acta.* **1997,** 1325, (2), 143-154.
79. Struck, D. K.; Hoekstra, D.; Pagano, R. E. *Biochemistry* **1981,** 20, (14), 4093-4099.
80. Moghimi, S. M.; Hunter, A. C.; Murray, J. C. *Pharmacol. Rev.* **2001,** 53, (2), 283-318.
81. Alexis, F.; Pridgen, E.; Molnar, L. K.; Farokhzad, O. C. *Mol. Pharm.* **2008,** 5, (4), 505-515.
82. Yoo, J. W.; Chambers, E.; Mitragotri, S. *Curr. Pharm. Des.* **2010,** 16, (21), 2298-2307.
83. Popović, Z.; Liu, W.; Chauhan, V. P.; Lee, J.; Wong, C.; Greytak, A. B.; Insin, N.; Nocera, D. G.; Fukumura, D.; Jain, R. K.; Bawendi, M. G. *Angew. Chem. Int. Ed.* **2010,** 49, (46), 8649-8652.
84. Zhu, Z.; Xie, C.; Liu, Q.; Zhen, X.; Zheng, X.; Wu, W.; Li, R.; Ding, Y.; Jiang, X.; Liu, B. *Biomaterials* **2011,** 32, (35), 9525-9535.
85. Schadlich, A.; Caysa, H.; Mueller, T.; Tenambergen, F.; Rose, C.; Gopferich, A.; Kuntsche, J.; Mader, K. *Acs Nano* **2011,** 5, (11), 8710-8720.
86. Geng, Y.; Dalhaimer, P.; Cai, S. S.; Tsai, R.; Tewari, M.; Minko, T.; Discher, D. E. *Nat. Nanotechnol.* **2007,** 2, (4), 249-255.
87. Christian, D. A.; Cai, S. S.; Garbuzenko, O. B.; Harada, T.; Zajac, A. L.; Minko, T.; Discher, D. E. *Mol. Pharm.* **2009,** 6, (5), 1343-1352.
88. Loverde, S. M.; Klein, M. L.; Discher, D. E. *Adv. Mater.* **2011,** 24, (28), 3823-3830.
89. Fox, M. E.; Szoka, F. C.; Fréchet, J. M. J. *Accounts. Chem. Res.* **2009,** 42, (8), 1141-1151.
90. Prencipe, G.; Tabakman, S. M.; Welsher, K.; Liu, Z.; Goodwin, A. P.; Zhang, L.; Henry, J.; Dai, H. J. *J. Am. Chem. Soc.* **2009,** 131, (13), 4783-4787.
91. Venkataraman, S.; Hedrick, J. L.; Ong, Z. Y.; Yang, C.; Ee, P. L. R.; Hammond, P. T.; Yang, Y. Y. *Adv. Drug Del. Rev.* **2011,** 63, (14-15), 1228-1246.
92. Giri, S.; Trewyn, B. G.; Stellmaker, M. P.; Lin, V. S. Y. *Angew. Chem. Int. Ed.* **2005,** 44, (32), 5038-5044.
93. Wijaya, A.; Schaffer, S. B.; Pallares, I. G.; Hamad-Schifferli, K. *Acs Nano* **2009,** 3, (1), 80-86.
94. Chauhan, V. P.; Popovic, Z.; Chen, O.; Cui, J.; Fukumura, D.; Bawendi, M. G.; Jain, R. K. *Angew. Chem. Int. Ed* **2011,** 50, (48), 11417-20.

95. Gratton, S. E. A.; Ropp, P. A.; Pohlhaus, P. D.; Luft, J. C.; Madden, V. J.; Napier, M. E.; DeSimone, J. M. *Proc. Natl. Acad. Sci. USA* **2008,** 105, (33), 11613-11618.
96. Petros, R. A.; DeSimone, J. M. *Nat. Rev. Drug Discov.* **2010,** 9, (8), 615-627.
97. Meng, H.; Yang, S.; Li, Z.; Xia, T.; Chen, J.; Ji, Z.; Zhang, H.; Wang, X.; Lin, S.; Huang, C.; Zhou, Z. H.; Zink, J. I.; Nel, A. E. *Acs Nano* **2011,** 5, (6), 4434-4447.
98. Takeoka, S.; Mori, K.; Ohkawa, H.; Sou, K.; Tsuchida, E. *J. Am. Chem. Soc.* **2000,** 122, (33), 7927-7935.
99. Pati, D.; Kalva, N.; Das, S.; Kumaraswamy, G.; Sen Gupta, S.; Ambade, A. V. *J. Am. Chem. Soc.* **2012,** 134, (18), 7796-802.
100. Fox, M. E.; Guillaudeu, S.; Frechet, J. M. J.; Jerger, K.; Macaraeg, N.; Szoka, F. C. *Mol. Pharm.* **2009,** 6, (5), 1562-1572.
101. O'Brien, M. E. R.; Wigler, N.; Inbar, M.; Rosso, R.; Grischke, E.; Santoro, A.; Catane, R.; Kieback, D. G.; Tomczak, P.; Ackland, S. P.; Orlandi, F.; Mellars, L.; Alland, L.; Tendler, C.; Grp, C. B. C. S. *Ann. Oncol.* **2004,** 15, (3), 440-449.
102. Gradishar, W. J.; Tjulandin, S.; Davidson, N.; Shaw, H.; Desai, N.; Bhar, P.; Hawkins, M.; O'Shaughnessy, J. *Journal of Clinical Oncology* **2005,** 23, (31), 7794-7803.
103. Sun, Q.; Radosz, M.; Shen, Y. *J. Control. Release* **2012,** 164, (2), 156-169.

**Key Research Accomplishments**

1. We used linear cationic polymer poly(ethyleneimine) (LPEI) as the charge-reversal polymers and demonstrated its breast-cancer-targeted nuclear drug delivery capability.

2. We synthesized polyhistine based conjugate as an efficient breast cancer cell-targeted charge-reversal drug-loaded nanoparticle for nuclear drug delivery to enhance the drug's cytotoxicity.

3. We prepared a negative-to-positive charge-reversal liposome for cancer drug targeted delivery. The charge reversal liposome could be effectively cellular internalized with higher cytotoxicity to cancer cells, showing a great promise for *in vivo* administrations.

4. Using TAT as an example, we demonstrated an efficient molecular modification approach that involves reversible blocking/activation of cationic CPPs. The amidized CPPs are very stable and have completely inhibited nonspecific interactions in the blood compartment. Thus, coupled with tissue-specific targeting groups, this approach may greatly widen the door for in vivo applications of CPPs.

5. We developed an efficient synthesis of monodispersed bis-MPA polyester dendrimers using thiol−acrylate reaction and the traditional esterification reaction under mild conditions. The simple synthesis and purification make the dendrimer synthesis straight forward for large-scale production.

6. We developed a convenient synthesis of interior-and-peripheral-bifunctionalized dendritic polymers. These bifunctional dendritic polymers are nontoxic and biodegradable, offering a versatile platform for various biomedical applications.

7. We developed a liposomal dendrimer nanoassembly (*DLC-PEG*) and demonstrated it can improve tumor accumulation, penetration, and cellular uptake. The "cluster bomb" concept may be a very promising approach uniting the needed properties for high chemotherapeutic efficacy.

8. We demonstrated a facile approach to fabricate polymer-drug conjugate nanorods for cancer-drug delivery. The nanorods with medium lengths (<500 nm) also had a much better stealth property and thus a much longer blood circulation time than the nanospheres.

**Reportable Outcomes**

1. Zhuxian Zhou, Youqing Shen, Jianbin Tang, Erlei Jin, Xinpeng Ma, Qihang Sun, Bo Zhang, Edward A. Van

Kirk and William J. Murdoch. Linear Polyethyleneimine-based Charge-Reversal Nanoparticles for Nuclear-Targeted Drug Delivery. Journal of Materials Chemistry, 2011, 21, 19114–19123.

2. Erlei Jin, Youqing Shen, Jianbin Tang, Zhuxian Zhou, Xinpeng Ma, Qihang Sun, Bo Zhang, Edward A. Van Kirk and William J. Murdoch. pH-Responsive Polyhistidine Nanoparticles for Nuclear Targeted Drug Delivery. Manuscript to be submitted.
3. Xinpeng Ma, Zhuxian Zhou, Bo Zhang, Erlei Jin, Qihang Sun, Jianbin Tang, Youqing Shen, Edward Van Kirk, William J. Murdoch, Maciej Radosz. Charge-Reversal Liposomes for Cancer Nuclear Targeted Drug Delivery. Manuscript to be submitted.
4. Erlei Jin, Bo Zhang, Xuanrong Sun, Zhuxian Zhou, Xinpeng Ma, Qihang Sun, Jianbin Tang, Youqing Shen, Edward Van Kirk, William J. Murdoch, Maciej Radosz. Acid-Active Cell-Penetrating Peptides for in Vivo Tumor-Targeted Drug Delivery. Journal of the American Chemical Society, 2013, 135, 933.
5. Xinpeng Ma, Jianbin Tang, Youqing Shen, Maohong Fan, Huadong Tang, Maciej Radosz. Facile Synthesis of Polyester Dendrimers from Sequential Click Coupling of Asymmetrical Monomers. Journal of the American Chemical Society, 2009, 131, 14795-14803.
6. Xinpeng Ma, Zhuxian Zhou, Erlei Jin, Qihang Sun, Bo Zhang, Jianbin Tang, Youqing Shen. Facile Synthesis of Polyester Dendrimers as Drug Delivery Carriers. Macromolecules, 2013, 46, 37.
7. Xinpeng Ma, Qihang Sun, Zhuxian Zhou, Erlei Jin, Jianbin Tang, Edward Van Kirk, William J. Murdoch, Youqing Shen. Synthesis of Degradable Bifunctional Dendritic Polymers as Versatile Drug Carriers. Polymer Chemistry, 2013, 4, 812.
8. Qihang Sun, Xinpeng Ma, Zhuxian Zhou, Erlei Jin, Bo Zhang, Youqing Shen, Edward Van Kirk, William J. Murdoch, Joseph R. Lott, Timothy P. Lodge, Maciej Radosz. Lipid/Dendrimer Nanoassembly as “Cluster Bomb” for Cascade Tumor Penetration. To be submitted to Nature Materials.
9. Zhuxian Zhou, Xinpeng Ma, Erlei Jin, Jianbin Tang, Youqing Shen, Edward Van Kirk, William J. Murdoch, Maciej Radosz. Linear-Dendritic Drug Conjugates Forming Long Circulating Nanorods for Cancer Drug Delivery. Biomaterials, 2013, 34, 5722.
10. Qihang Sun, Maciej Radosz, Youqing Shen. Challenges in design of translational nanocarriers. Journal of Controlled Release, 2012, 164, 156.